

XMM-Newton observations of GX 13+1: correlation between photoionised absorption and broad line emission

M. Díaz Trigo¹, L. Sidoli², L. Boirin³, and A.N. Parmar⁴

¹ ESO, Karl-Schwarzschild-Strasse 2, D-85748 Garching bei München, Germany

² INAF-IASF, via Bassini 15, I-20133 Milano, Italy

³ Observatoire Astronomique de Strasbourg, 11 rue de l'Université, F-67000 Strasbourg, France

⁴ ESAC, P.O. Box 78, E-28691 Villanueva de la Cañada, Madrid, Spain

Received ; Accepted:

Abstract. We analysed data from five XMM-Newton observations of GX 13+1 to investigate the variability of the photo-ionised absorber present in this source. We fitted EPIC and RGS spectra obtained from the “least-variable” intervals with a model consisting of disc-blackbody and blackbody components together with a Gaussian emission feature at ~ 6.55 – 6.7 keV modified by absorption due to cold and photo-ionised material. We found a significant correlation between the hard, ~ 6 – 10 keV, flux, the ionisation and column density of the absorber and the equivalent width of the broad iron line. We interpret the correlation in a scenario in which a disc wind is thermally driven at large, $\sim 10^{10}$ cm, radii and the broad line results from reprocessed emission in the wind and/or hot atmosphere. The breadth of the emission line is naturally explained by a combination of scattering, recombination and fluorescence processes. We attribute the variations in the absorption and emission along the orbital period to the view of different parts of the wind, possibly located at slightly different inclination angles. We constrain the inclination of GX 13+1 to be between 60 and 80° from the presence of strong absorption in the line of sight, that obscures up to 80% of the total emission in one observation, and the absence of eclipses. We conclude that the presence of a disc wind and/or a hot atmosphere can explain the current observations of narrow absorption and broad iron emission features in neutron star low mass X-ray binaries as a class.

Key words. X-rays: binaries – Accretion, accretion disks – X-rays: individual: GX 13+1

1. Introduction

GX 13+1 is a type I X-ray burster (Fleischman 1985; Matsuba et al. 1995) with a bright persistent X-ray emission. It is associated with an evolved late-type K5 III star, located at a distance of 7 ± 1 kpc (Bandyopadhyay et al. 1999). GX 13+1 is the most luminous “atoll” source known to date, with an intermediate luminosity (~ 0.1 Eddington luminosity) between the so-called “Z” Low Mass X-ray Binaries (LMXBs) and all other “atoll” sources. Its nature has been debated in the literature since it shows some features from Z sources, like 57–69 QPOs (Homan et al. 1998), persistent radio emission (Grindlay & Seaquist 1986) and high accretion rate, and some proper from atoll sources (e.g. the path in the colour-colour diagram). The investigation of the aperiodic variability of bright persistent X-ray sources led Reig et al. (2003) to propose a new classification for LMXBs, depending on the rms amplitude and the slope of their power density spectra. In their scheme, GX 13+1 is the only “atoll” source which has been classified as a type I source (lower rms, $\text{rms} < 20\%$, and flatter power spectra, $\alpha < 0.9$), a class

which includes all the “Z” sources. Schnerr et al. (2003) proposed to explain the source peculiar spectral and power spectral properties with the presence of a relativistic jet. Paizis et al. (2006) first detected a hard X-ray tail in the GX 13+1 average hard X-ray spectrum (> 20 keV), summing together all the available INTEGRAL observations. They found a correlation for “Z” sources and bright “GX” atolls (like GX 13+1), between the X-ray hard tail (40–100 keV) and their radio luminosity, likely indicating that hard tails and energetic electrons causing the radio emission may have the same origin, most likely the Compton cloud located inside the neutron star (NS) magnetosphere.

Corbet (2003) found a modulation of 24.065 ± 0.018 d in RXTE ASM data spanning 7 years and suggested that this may be the orbital period of the system. A similar modulation was found by Bandyopadhyay et al. (2002) after performing infrared photometry of the source. The 24 day period has been recently confirmed from both the K-band and additional X-ray observations (Corbet et al. 2010). Other NIR observations (Froning et al. 2008) show that the accretion disc is the dominant emitter in GX 13+1

($\sim 3/4$ of NIR flux comes from the disc at the time of those observations).

Ueda et al. (2001) discovered narrow resonant absorption lines near 7 keV from GX 13+1 using ASCA. The same features were studied with XMM-Newton by Sidoli et al. (2002) who found a complex of features identified with resonant scattering from the $K\alpha$ and $K\beta$ lines of He- and H-like iron (Fe XXV and Fe XXVI), H-like calcium (Ca XX) $K\alpha$ as well as the presence of a deep ($\tau \sim 0.2$) Fe XXV absorption edge at 8.83 keV. The absorption lines were superposed on a broad emission feature whose energy and breadth were poorly determined, partly due to the presence of the deep Fe $K\alpha$ features. *Chandra* HETGS observations (Ueda et al. 2004) revealed that the features are blue-shifted indicating an outflowing plasma with a velocity of $\sim 400 \text{ km s}^{-1}$.

GX 13+1 is unusual in that all the other LMXB systems that exhibit prominent Fe XXV and Fe XXVI features are dipping sources (see Table 5 of Boirin et al. 2004). Dipping sources are LMXB systems that are observed from close to the plane of the accretion. The dips are believed to be caused by periodic obscuration of the central X-ray source by structure located in the outer regions of a disc (White & Swank 1982). The depth, duration and spectral evolution of the dips varies from source to source and often from cycle to cycle. The lack of an orbital modulation of the absorption features outside of the dips indicates that the absorbing plasma is located in a cylindrical geometry around the compact object. The important role that photo-ionised plasmas play in LMXBs was recognised by Boirin et al. (2005) and Díaz Trigo et al. (2006) who were able to model the changes in *both* the narrow X-ray absorption features and the continuum during the dips from all the bright dipping LMXB observed by XMM-Newton by an increase in the column density and a decrease in the amount of ionisation of a photo-ionised absorbing plasma. Since dipping sources are normal LMXBs viewed from close to the orbital plane, this implies that photo-ionised plasmas are common features of LMXBs. Outside of the dips, the properties of the absorbers do not vary strongly with orbital phase suggesting that the ionised plasma has a cylindrical geometry with a maximum column density close to the plane of the accretion disc.

Since GX 13+1 exhibits deep Fe absorption features similar to the dipping LMXBs, this suggests that GX 13+1 may be a high-inclination LMXB and that as such the overall X-ray continuum may be similarly affected. To investigate the origin of the variability of the absorption and the presence of dipping activity, we successfully applied for five observations of GX 13+1 with XMM-Newton, spaced by at least one day. In this paper, we report on this monitoring program. We include results from the RGS detectors and the optical monitor, which were not reported for the early 2000 observations.

2. XMM-Newton observations

The XMM-Newton Observatory (Jansen et al. 2001) includes three 1500 cm^2 X-ray telescopes each with an EPIC (0.1–15 keV) at the focus. Two of the EPIC imaging spectrometers use MOS CCDs (Turner et al. 2001) and one uses pn CCDs (Strüder et al. 2001). The RGSs (0.35–2.5 keV, Den Herder et al. 2001) are located behind two of the telescopes. In addition, there is a co-aligned 30 cm diameter Optical/UV Monitor telescope (OM, Mason et al. 2001), providing simultaneously coverage with the X-ray instruments. Data products were reduced using the Science Analysis Software (SAS) version 10.0. The EPIC MOS cameras were not used during the observation in order to allocate their telemetry to the EPIC pn camera and avoid Full Scientific Buffer in the latter. We present here the analysis of EPIC pn data, RGS data from both gratings and OM data.

Table 1 is a summary of the XMM-Newton observations. We used the EPIC pn in timing mode. In this mode only one CCD chip is operated and the data are collapsed into a one-dimensional row (4'4) and read out at high speed, the second dimension being replaced by timing information. This allows a time resolution of $30 \mu\text{s}$. We used the SAS task **epfast** on the event files to correct for a Charge Transfer Inefficiency (CTI) effect which has been observed in EPIC pn timing mode when high count rates are present¹. Ancillary response files were generated using the SAS task **arfgen** following the recommendations of the *XMM-Newton SAS User guide* for piled-up observations in timing mode, whenever applicable. Response matrices were generated using the SAS task **rmfgen**.

Light curves were generated with the SAS task **epiclccorr**, which corrects for a number of effects like vignetting, bad pixels, PSF variation and quantum efficiency and accounts for time dependent corrections within a exposure, like dead time and GTIs.

The SAS task **rgsproc** was used to produce calibrated RGS event lists, spectra, and response matrices. We also chose the option *keepcool=no* to discard single columns that give signals a few percent below the values expected from their immediate neighbours. Such columns are likely to be important when studying weak absorption features in spectra with high statistics. We used the SAS task **rgsbkgmodel** to compute model background spectra from RGS background templates. We generated RGS light curves with the SAS task **rgslccorr**.

The OM was operated in image+fast mode. The U, UVW1 and UVM2 filters were used. In this mode the instrument produces images of the entire $17' \times 17'$ FOV with a time resolution between 800 and 5000 s and event lists with a time resolution of 0.5 s from a selected $11'' \times 11''$ region. The SAS task **omfchain** was used to extract

¹ More information about the CTI correction can be found in the *EPIC status of calibration and data analysis* and in the Current Calibration File (CCF) release note *Rate-dependent CTI correction for EPIC-pn timing modes*, by Guainazzi et al. (2009), at http://xmm.esac.esa.int/external/xmm_calibration

Table 1. XMM-Newton observations of GX 13+1. Results from the first three observations are reported in Sidoli et al. (2002). T is the total EPIC pn exposure time and C is the pn 0.6–10 keV total count rate after dead time correction. In all cases the EPIC pn thin filter was used. For obs 5 only RGS and OM data are available.

Obs Num	Observation ID	Observation Times (UTC)			T (ks)	C (s ⁻¹)
		Start		End		
		(year month day)	(hr:mn)	(hr:mn)		
1	0122340101	2000 March 30	14:10	16:58	6.0	674
2	0122340901	2000 April 01	04:29	07:54	8.1	781
3	0122341001	2000 April 01	08:51	11:16	4.6	690
4	0505480101	2008 March 09	15:48	22:50	22.9	843
5	0505480701	2008 March 11	19:00	23:10	12.0	—
6	0505480201	2008 March 11	23:10	27:16	12.4	909
7	0505480301	2008 March 22	02:20	07:15	15.3	818
8	0505480501	2008 March 25	23:01	26:59	11.9	761
9	0505480401	2008 September 5	21:49	26:48	15.5	746

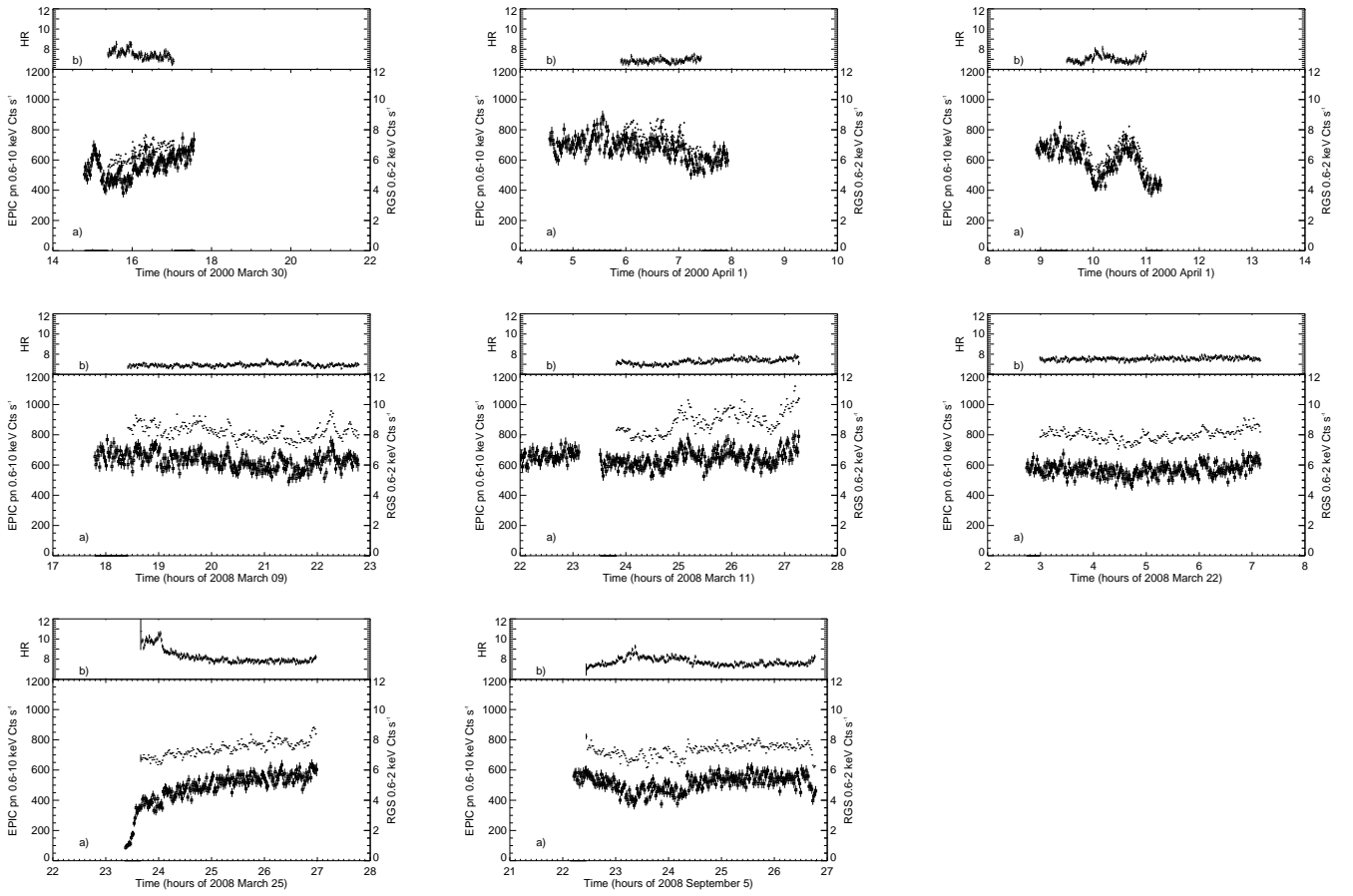


Fig. 1. a) 0.6–10 keV EPIC pn (dots) and 0.6–1.8 keV RGS (squares) background subtracted light curves for each GX 13+1 observation with a binning of 64 s. The left (right) axes show the scale for EPIC pn (RGS). b) Hardness ratio (counts in the 2–10 keV band divided by those between 0.6–2 keV) for the EPIC pn light curves.

light curves of GX 13+1 from the high time resolution fast mode data. We used a time sampling of 100 s in the curve extraction to improve the signal-to-noise ratio.

2.1. Pile-up and X-ray loading in the EPIC pn camera

The count rate in the EPIC pn was close to, or above, the 800 counts s⁻¹ level, at which X-ray loading and pile-up effects become significant.

Pile-up occurs when more than one photon is read in a pixel during a read-out cycle. This causes photon loss, pattern migration from lower to higher pattern types and hardening of the spectrum, because the charge deposited by more than one photon is added up before being read out². In addition, when high count rates are present, the offset map calculated at the beginning of an exposure may be contaminated by X-ray events from the source, the so-called “X-ray loading”. As a consequence pattern migration from higher to lower pattern types and a shift to lower energy for all the events associated with the contaminated pixel occur³. Since both X-ray loading and pile-up cause significant spectral distortion, we investigated in detail their presence before extracting the spectra.

We used the SAS task `epatplot`, which utilizes the relative ratios of single- and double-pixel events which deviate from standard values in case of significant pile-up, as a diagnostic tool in the pn camera timing mode data and found that all the spectra were affected by pile-up. Next, we extracted several spectra selecting single and double timing mode events (patterns 0 to 4) but different spatial regions for the source. Source events were first extracted from a $62''$ (15 columns) wide box centred on the source position (Region 1). Next we excluded 1, 3, 5 and 7 columns from the centre of Region 1 (Regions 2–5) and extracted one spectrum for each of the defined regions. We obtained spectra free of pile-up once events within the inner 5 columns were excluded.

Next, we inspected the pn offset maps to diagnose the presence of X-ray loading. For each observation, we calculated the so-called “residual” offset map by subtracting the offset map of a nearby observation taken with closed filter from the offset map of the observation. We found that all the observations showed effects of X-ray loading in at least the inner 5 columns of the PSF. X-ray loading could be significant in the inner 7 columns, but the noise fluctuations in the individual rows for outer columns are of the order of the level of excess in the 6th and 7th columns. Therefore, we extracted the final spectra after excluding events from the central 5 columns.

2.2. Background subtraction

In the EPIC pn timing mode, there are no source-free background regions, since the PSF of the telescope extends further than the central CCD boundaries. The central CCD has a field of view of $13'6 \times 4'4$ in the pn. In timing mode, the largest column is the one in which the data are collapsed into one-dimensional row. Therefore, the maximum angle for background extraction is $2'$, compared to $5'$ for imaging modes. Since GX 13+1 is very bright, its spectrum will not be significantly modified by the “real”

background which contributes less than 1% to the total count rate in most of the bandwidth. Conversely, subtracting the background extracted from the outer columns of the central CCD will modify the source spectrum, since the PSF is energy dependent and the source photons scattered to the outer columns do not show the same energy dependence as the photons focused on the inner columns. Therefore, we chose not to subtract the “background” extracted from the outer regions of the central CCD (see also Done & Díaz Trigo 2010; Ng et al. 2010). We expect a contribution from the background to the total count rate of more than 1% below 1.7 keV. Therefore, below this energy we used only the RGS spectra, for which background templates were available.

3. Light curves

3.1. EPIC pn and RGS light curves

Figure 1 shows 0.6–10 keV EPIC pn and 0.6–1.8 keV RGS light curves of five XMM-Newton observations of GX 13+1 performed in 2008 together with three observations performed in 2000, for comparison, with a binning of 64 s.

The EPIC pn light curves are remarkably similar to the simultaneous RGS light curves despite the different energy band. We note that the lower RGS count rate with respect to the pn count rate in the 2008 observations compared to the 2000 observations is due to the inoperative CCDs 7 (RGS1) and 4 (RGS2) since early after the beginning of the mission. A high variability is present in all the observations. The average count rate changes significantly from one observation to the next one, with values between ~ 700 and $900 \text{ counts s}^{-1}$. The count rate variability is not associated to significant changes in the spectral hardness for obs 4 and 6. However, obs 1, 3, 8 and 9 show spectral hardening associated with a decrease of count rate. Obs 6 shows the highest count rate, with peaks of up to $\sim 1100 \text{ counts s}^{-1}$ in the EPIC pn camera. Obs 8 shows the lowest count rate, with less than 1 counts s^{-1} at the beginning of the observation in the RGS, compared to $\sim 6 \text{ counts s}^{-1}$ at the end of the observation. This behaviour could be related to dipping activity. Obs 9 shows a decrease of count rate at ~ 23 – 24.5 h which is related to spectral hardening and could be again an indication for dipping behaviour in GX 13+1.

We next examined the hardness ratio (counts in the 2–10 keV band divided by those between 0.6–2 keV) as a function of 0.6–10 keV count rate for all the observations (Fig. 2). The largest hardness ratios correspond to the intervals of low count rate present in obs 1, 3, 8 and 9. This behaviour is typical of deep dipping states of dipper. A detailed comparison of Fig. 2 with Fig. 4 from Boirin et al. (2005) shows that indeed obs 1, 3, 8 and 9 occupy the same parameter space in the figure as the deep dipping state of 4U 1323–62, while obs 2, 4 and 7 resemble the shallow dipping states and obs 6 the persistent state. We analyse in detail the origin of these states in Sect. 4.1.4.

² See *XMM-Newton Users Handbook* for more information on pile-up.

³ More information about X-ray loading can be found in the *PN X-ray loading investigation results* calibration document by Smith (2004) at <http://xmm.esac.esa.int>

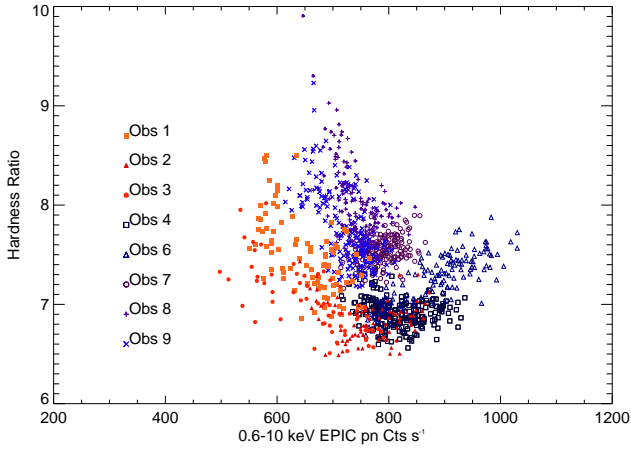


Fig. 2. Hardness ratio (2–10 keV/0.6–2 keV counts) versus 0.6–10 keV EPIC pn count rate for all the observations. Data from obs 1 to 3 are shown as filled squares, filled triangles and filled circles, respectively. Data from obs 4 and 6 to 9 are shown as open squares, open triangles, open circles, crosses and crooked crosses, respectively. Each point corresponds to a binning of 64 s.

3.2. Light curves from other X-ray missions

In order to investigate the variability of GX 13+1 further, we extracted from the High Energy Astrophysics Science Archive Research Center (HEASARC) light curves from previous GX 13+1 X-ray observations with the maximum time resolution available. We did not perform a systematic search of dips in all the GX 13+1 archival observations. Instead, we looked for the signature of dipping episodes in observations where a “bi-modal” behaviour of the count rate with hardness ratio had been reported in the literature (Stella et al. 1985; Schnerr et al. 2003). Our goal was to determine if dipping behaviour may have been not recognized in previous observations of GX 13+1 and to see if such dipping behaviour, if existent, is associated with a certain state of the source.

Details on the observations of GX 13+1 from archival X-ray observations which may show dipping behaviour are given in Table 2. The light curve corresponding to the RXTE observation is shown in Fig. 3. The light curve from the EXOSAT archival observation is shown in Fig. 1 from Stella et al. (1985). In both observations a decrease of count rate, which is more pronounced in the soft band, is visible. The decrease in the 1–4 keV EXOSAT (2–4 keV RXTE) light curves is ~ 25 –30% and is accompanied by spectral hardening.

Finally we examined the GX 13+1 RXTE All-Sky Monitor (ASM) 1.5–12 keV light curves spanning more than 13 years and with a time resolution of 96 s to search for any characteristic signature at the time of appearance of dips. We corrected the ASM light curves to the solar system barycentre using the FTOOL task `fbary` and folded the light curves into segments between 0.1 and 24 days duration, but clear dipping activity was not detected. A

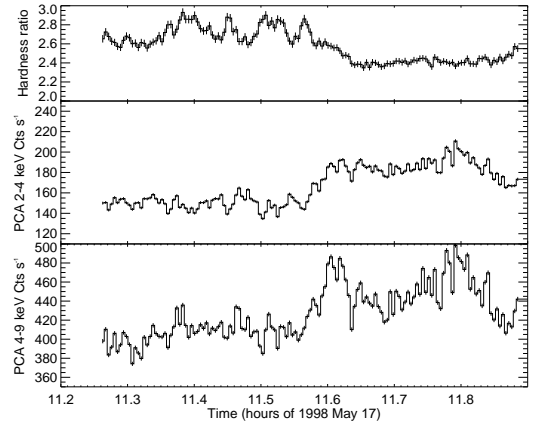


Fig. 3. 2–4 keV (middle) and 4–9 keV (bottom) RXTE PCA background subtracted light curves for an archival GX 13+1 observation with a binning of 16 s. *Top:* Hardness ratio (counts in the 4–9 keV band divided by those between 2–4 keV) for the RXTE PCA light curves shown in the middle and bottom panels.

Table 2. X-ray archival observations of GX 13+1 with potential dip states.

Date	Mission	Reference
1983 September 22	EXOSAT	Stella et al. (1985)
1998 May 17	RXTE	Schnerr et al. (2003)

modulation of the ASM data has been already extensively searched and it is reported in the literature (Corbet 2003; Corbet et al. 2010). Therefore, we did not look further for periodic behaviour in the ASM data.

4. X-ray spectra

We extracted EPIC pn and RGS spectra for each observation. We rebinned the EPIC pn spectra to over-sample the *FWHM* of the energy resolution by a factor 3 and to have a minimum of 25 counts per bin, to allow the use of the χ^2 statistic. To account for systematic effects we added a 0.8% uncertainty to each spectral bin after rebinning (we note that this is equivalent to add $\sim 2\%$ uncertainty to each spectral bin before rebinning). We used the RGS spectra with two different binnings: in Sect. 4.1 we rebinned the RGS spectra to have a minimum of 25 counts per bin, to be able to consistently use the χ^2 statistic for both EPIC pn and RGS spectra. In Sect. 4.2 we rebinned the RGS spectra to over-sample the *FWHM* of the energy resolution by a factor 3 to be sensitive to narrow features and we used the C-statistic (Cash 1979). We performed spectral analysis using XSPEC (Arnaud 1996) version 12.6.0q. Since there were no photons in the RGS spectra below ~ 0.8 keV, we used the RGS spectra in the energy interval 0.8–1.8 keV. We used the pn spectra be-

tween 1.7 and 10 keV in order to exclude energy bins for which we expect the spectrum to be affected by background (see Sect. 2.2). To account for absorption by neutral gas we used the `tbabs` XSPEC model with solar abundances (Anders & Grevesse 1989). Spectral uncertainties are given at 90% confidence ($\Delta\chi^2 = 2.71$ for one interesting parameter), and upper limits at 95% confidence.

We extracted intervals of low variability for all the observations, using as a criterion the hardness ratio and the count rate of the observations. For obs 7 there are no significant variations of hardness ratio or count rate during the observation. Therefore we only consider one interval for this observation. We divided obs 4, 6, 8 and 9 in two intervals each (“high” and “low”) and examined the spectra separately. A quick look shows that while for obs 4, 8 and 9 both intervals show significant spectral changes, the two intervals of obs 6 are only different in the normalisation factors. Therefore we continued the analysis for obs 6 only with one interval. We continued the analysis for obs 4, 8 and 9 only with the “high”, less variable, intervals, for which we could accumulate a sufficient, > 5 ks, net exposure time.

4.1. EPIC and RGS spectral analysis

4.1.1. Phenomenological model

We first examined the spectra of the low-variability interval separately for each observation. We combined the RGS spectra (RGS1 and RGS2, order 1) and the EPIC pn spectrum and fitted them with a model consisting of a disc blackbody and a blackbody components modified by neutral material. A constant factor, fixed to 1 for the pn spectrum, but allowed to vary for each RGS spectrum, was included multiplicatively in order to account for cross-calibration uncertainties.

The residuals showed strong absorption lines near 7 keV superposed on a broad emission feature and weak absorption features at ~ 1.8 and 2.3 keV. The latter are most likely due to residual calibration uncertainties (after using the SAS task `epfast`), due to an incorrect application of the CTI correction in the EPIC pn camera when high count rates are present⁴. We modeled such features with two Gaussian absorption components and do not discuss them further. However, we note that these features, if due to residual uncertainties of the CTI correction, indicate that the energy gain could be compromised in the whole energy band. Detailed plots of the residuals from the best-fit continuum model around the Fe K region are shown in Fig. 4. Absorption features from highly ionised

species of iron, such as Fe XXV and Fe XXVI $K\alpha$ and $K\beta$ are evident. A broad iron emission line is present in all the observations. Both the absorption and emission features show significant variations among observations, with obs 6 and 7 showing the most ionised species in absorption and the weakest line in emission. Obs 4 and 9 show the strongest line in emission and a prominent absorption edge at ~ 9 keV, that we identify with absorption from Fe XXV and Fe XXVI.

We first evaluated the effect of the continuum in the absorption and emission features in a model-independent manner calculating the ratio among the spectra for all the observations with respect to obs 6 (see Fig. 5). Obs 7 shows a similar spectral shape to obs 6 and a flux lower by $\sim 10\%$ in all the energy band. Above ~ 6 keV, obs 4, 8 and 9 show a significant deficit of photons with respect to obs 6 and 7. Below ~ 5 keV, obs 8 and 9 show the lowest fluxes. Interestingly, obs 4 shows the lowest 6–10 keV flux of all the observations but the highest 1.5–5 keV flux together with obs 6. This analysis indicates that the hard, ~ 6 –10 keV, flux could be correlated with the ionisation of the absorption features and the significance of the broad emission line. As the hard flux increases from obs 4 to obs 9, 7 and 6 the significance of the broad emission line decreases and the absorption features become weaker and reveal an increase of ionisation in the plasma. Obs 8 shows an intermediate hard flux and broad emission line, but the less ionised absorption features, indicating that the flux below ~ 5 keV may play an important role in the ionisation of the absorbing plasma.

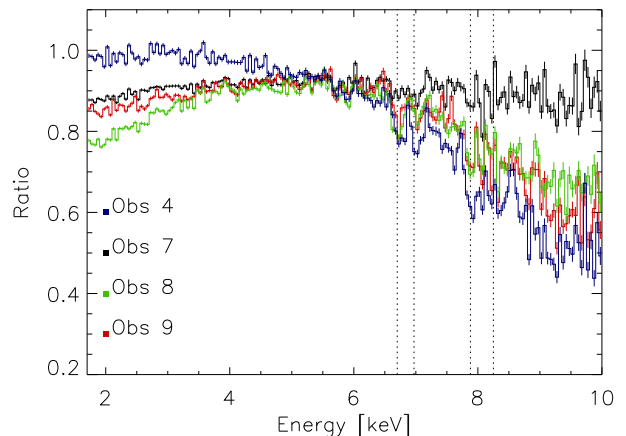


Fig. 5. Ratio of EPIC pn GX 13+1 spectra from obs 4, 7, 8 and 9 with respect to obs 6.

⁴ We note that while the use of `epfast` is recommended by the EPIC calibration team, the recent discovery that the count-rate dependency of the CTI may be caused by X-ray loading implies that the `epfast` correction may improve, but not completely solve, the CTI calibration deficiency (for more details, see “Evaluation of the spectral calibration accuracy in EPIC-pn fast modes” at http://xmm.esac.esa.int/external/xmm_calibration).

In order to quantify the relation between the significance of the emission and absorption features and the changes in the continuum, we next included in the model Gaussian absorption and emission features and absorption edges to account for the residuals near 7 keV. The total model consisted of disc blackbody and blackbody components, one Gaussian emission feature at

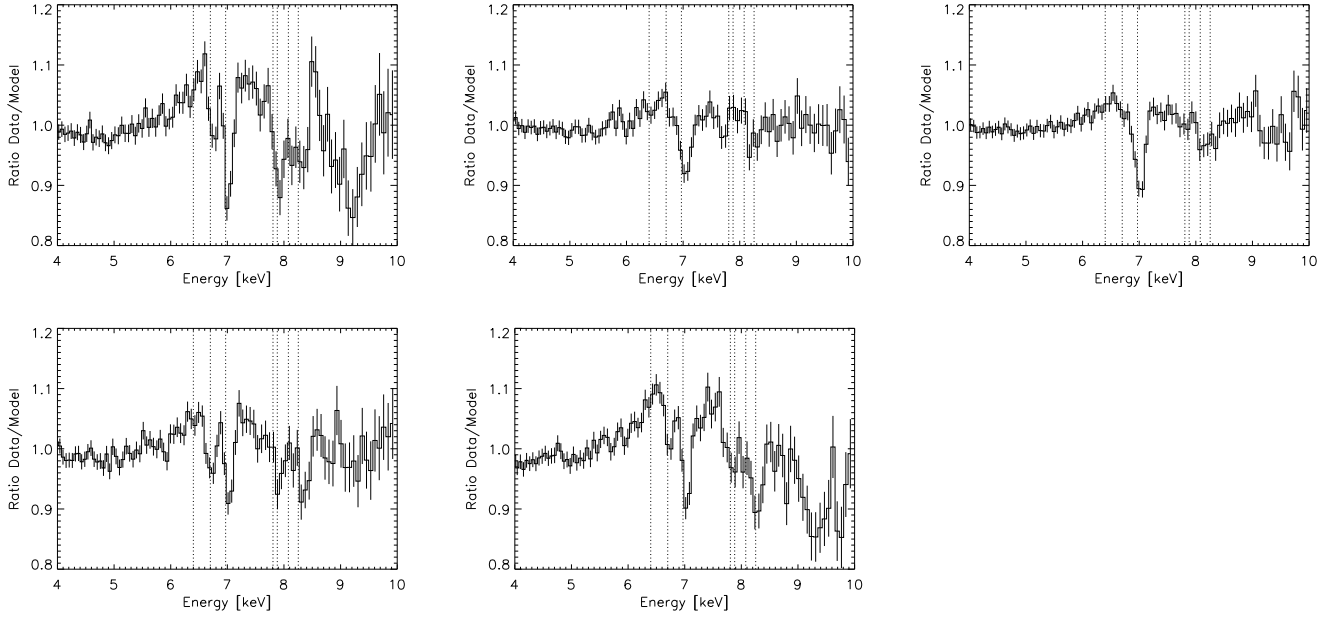


Fig. 4. Ratio of the data to the continuum model at the Fe K region for obs 4 (upper-left), 6 (upper-middle), 7 (upper-right), 8 (lower-left) and 9 (lower-middle). The dotted vertical lines indicate from left to right the rest energy of the transitions of neutral Fe, Fe XXV K α , Fe XXVI K α , Ni XXVII, Fe XXV K β , Ni XXVIII and Fe XXVI K β .

~ 6.6 keV and four Gaussian absorption features at the energies of Fe XXV and Fe XXVI K α and K β , modified by photo-electric absorption from neutral material and by absorption edges at the energies of Fe XXV and Fe XXVI ($\text{tbabs}*\text{edge}_1*\text{edge}_2*(\text{diskbb}+\text{bbodyrad}+\text{gau}_1+\text{gau}_2+\text{gau}_3+\text{gau}_4+\text{gau}_5)$, hereafter Model 1). The fits with Model 1 were acceptable, with χ^2_ν between 1.0 and 1.2 for ~ 530 – 700 d.o.f. for obs 4–9. The parameters of the Gaussian emission and absorption features and edges for the best-fit with this model are given in Table 3.

We can infer some properties of the absorber from the equivalent width (EW) of the absorption features, the depth of the edges and the predominance of a given ion. For example, the depth of the Fe XXV edge indicates that obs 4 and 9 have a column density of ionised plasma significantly larger than obs 6–8. The ratio of the Fe XXV and Fe XXVI K α to K β lines in obs 4 shows saturation of the lines, indicating most likely a column density above 10^{23} atom cm^{-2} ⁵. The ratio of the EW of the Fe XXV to Fe XXVI lines determines the ionisation of the plasma and shows that obs 6 and 7 have a very ionised plasma and that obs 8 has the least ionised plasma. Confirmation of the ionisation is given by the presence of low significance absorption features at ~ 1.88 keV in obs 8 and 9, that we identify with Si XIII, and at ~ 2.62 keV in obs 4, 8 and 9, that we identify with S XVI. Obs 8 shows also small features at ~ 2.0 , 2.5 and 4.2 keV that we identify with Si XIV, S XV and Ca XX. Taking the above into account we can also examine the relation between emission and ab-

sorption lines. The EW of the broad emission line is correlated with the EW of the narrow absorption lines (see Fig. 6). Obs 6 and 7 show the smallest emission line and the thinnest absorbing plasma. Obs 4 and 9 show instead the largest emission lines together with the largest column density of ionised plasma. The EW of the emission and absorption lines for obs 8 are intermediate between obs 4 and 9 on one side and obs 6 and 7 on the other side. Finally, the column density of the ionised plasma increases as the plasma becomes less ionised for obs 4, 6, 7 and 9. This is expected since obs 6 and 7 are likely to have a fraction of fully ionised plasma that reveals itself only through electron scattering. Instead, for obs 8 the decrease in the column density with respect to obs 4 and 9 cannot be explained simply by a change in ionisation and indicates that at the time of obs 8 a smaller column density is present.

4.1.2. Photoionised plasma model

The strength of the absorption features shown in Table 3 indicates that the continuum may be significantly affected by the absorbing plasma. Therefore, to quantify the above changes in a more physical manner, we substituted the absorption features and edges by the component **warmabs**, which models the absorption due to a photoionised plasma in the line of sight. This component not only accounts for the narrow absorption features evident near 7 keV but also modifies the overall continuum shape at regions where the spectral resolution is not enough to resolve individual features. We note that the **warmabs** model does not include Compton scattering, in contrast to the **xabs**

⁵ The exact column density at which the absorption lines reach saturation depends on the velocity broadening of the lines (see e.g. Fig. 1 of Tombesi et al. 2011).

Table 3. Parameters of the most significant absorption lines and edges and of the broad emission line detected in the EPIC pn spectra of obs 4–9. *f* indicates that a parameter was fixed. The width of the absorption features was constrained to be $\lesssim 0.1$ keV and of the broad emission feature to $\lesssim 1$ keV. *p* indicates that the error of a parameter pegged at the limit imposed. **gau**₁ corresponds to the broad emission feature and **gau**₂–**gau**₅ to narrow absorption features. The energy of the Fe XXV feature of obs 7 was unconstrained due to its low significance. Therefore, we fixed its energy considering that it would show a similar blueshift as the Fe XXVI feature for the same observation.

Observation No.	4	6	7	8	9
Comp.					
Parameter					
gau ₁					
E_{gau} (keV)	$6.53^{+0.11}_{-0.09}$	6.63 ± 0.13	$6.60^{+0.10}_{-0.14}$	$6.65^{+0.08}_{-0.11}$	6.71 ± 0.08
σ (keV)	$0.72^{+0.14}_{-0.16}$	0.74 ± 0.19	$0.62^{+0.20}_{-0.09}$	0.61 ± 0.18	$0.60^{+0.13}_{-0.11}$
k_{gau} (10^{-3} ph cm $^{-2}$ s $^{-1}$)	12 ± 4	8 ± 2	6 ± 3	9 ± 2	11 ± 2
EW (eV)	185 ± 62	108 ± 27	84 ± 42	139 ± 31	177 ± 32
gau ₂					
E_{gau} (keV)	$6.75^{+0.02}_{-0.05}$	–	6.73 (f)	6.71 ± 0.02	6.73 ± 0.02
σ (keV)	< 0.04	–	$0.008^{+0.002p}_{-0.008}$	< 0.07	< 0.05
k_{gau} (10^{-4} ph cm $^{-2}$ s $^{-1}$)	12 ± 3	–	4 ± 3	16^{+4}_{-8}	14 ± 4
EW (eV)	20 ± 5	–	6 ± 5	24^{+6}_{-12}	21 ± 6
gau ₃					
E_{gau} (keV)	7.02 ± 0.06	7.03 ± 0.02	7.00 ± 0.01	7.02 ± 0.02	7.03 ± 0.01
σ (keV)	< 0.03	0.07 ± 0.05	< 0.06	< 0.04	< 0.06
k_{gau} (10^{-4} ph cm $^{-2}$ s $^{-1}$)	23 ± 4	20 ± 5	22 ± 3	18 ± 4	24^{+4}_{-6}
EW (eV)	41 ± 7	30 ± 8	34 ± 5	32 ± 7	42^{+7}_{-11}
gau ₄					
E_{gau} (keV)	$7.91^{+0.46}_{-0.15}$	–	–	7.91 ± 0.05	$7.84^{+0.10}_{-0.06}$
σ (keV)	$0.003^{+0.007p}_{-0.003}$	–	–	$0.005^{+0.095p}_{-0.005}$	$0.03^{+0.07p}_{-0.03}$
k_{gau} (10^{-4} ph cm $^{-2}$ s $^{-1}$)	11 ± 4	–	–	5 ± 3	5 ± 4
EW (eV)	33 ± 12	–	–	15 ± 9	13 ± 10
gau ₅					
E_{gau} (keV)	$8.24^{+0.04}_{-0.06}$	–	8.20 ± 0.10	8.34 ± 0.05	8.26 ± 0.04
σ (keV)	$0.1^{+0p}_{-0.1p}$	–	$0.1^{+0p}_{-0.1p}$	< 0.097	$0.02^{+0.08p}_{-0.02p}$
k_{gau} (10^{-4} ph cm $^{-2}$ s $^{-1}$)	10 ± 4	–	6 ± 3	5 ± 2	7 ± 3
EW (eV)	37 ± 15	–	15 ± 8	18 ± 7	25 ± 11
edge ₁					
E (keV)	8.83 (f)	8.83 (f)	8.83 (f)	8.83 (f)	8.83 (f)
τ	0.18 ± 0.03	< 0.04	< 0.04	< 0.05	0.08 ± 0.04
edge ₂					
E (keV)	9.28 (f)	9.28 (f)	9.28 (f)	9.28 (f)	9.28 (f)
τ	< 0.03	0.04 ± 0.03	0.04 ± 0.03	< 0.05	< 0.09
χ^2_{ν} (d.o.f.)	1.08 (574)	1.11 (694)	1.03 (678)	1.07 (530)	1.18 (561)

model in the SPEX package (Kaastra et al. 1996). The contribution of Compton scattering is expected to be significant when modeling the changes between persistent and dipping emission (Boirin et al. 2005; Díaz Trigo et al. 2006). Therefore we added the component **cabs** to the model, which accounts for non-relativistic, optically-thin Compton scattering. We forced the column density of the **cabs** model to be equal to the column density of the **warmabs** component multiplied by a factor of 1.21. The latter factor accounts for the number of electrons per hydrogen atom for a material of solar abundances (Stelzer et al. 1999). The non-relativistic approximation

of **cabs** will overestimate the scattering fraction at high energies, and therefore it should not be used when broad band energy data is available. Moreover, the column density of the **warmabs** component sets only a lower limit to the amount of Compton scattering since there may be fully ionised material which cannot be identified via line absorption but still contributes to Compton scattering.

Our final model consisted of disc blackbody and blackbody components and one Gaussian emission feature at ~ 6.6 keV, modified by photoelectric absorption from neutral and ionised material

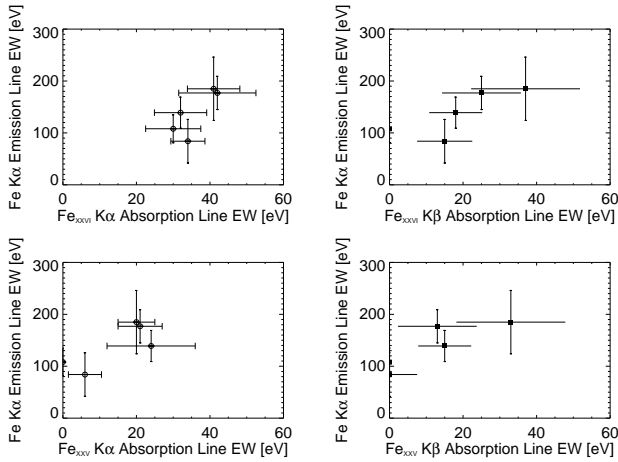


Fig. 6. EW of the broad emission line with respect to the narrow absorption lines of Fe XXVI K α (upper-left), Fe XXVI K β (upper-right), Fe XXV K α (lower-left) and Fe XXV K β (lower-right).

(tbabs*cabs*warmabs*(diskbb+bbodyrad+gau), hereafter Model 2).

The fits with Model 2 were acceptable, with χ^2_ν between 1.0 and 1.2 for ~ 550 – 700 d.o.f. for obs 4–9. The parameters of the best-fit with this model are given in Table 4 and the residuals of the fit and unfolded spectra are shown in Figs. 7 and 8. For each observation, we used the best-fit continuum before adding the broad emission line and the photo-ionised absorber as an ionising continuum for the latter. The density of the plasma was set to be $n = 10^{13} \text{ cm}^{-3}$ following Ueda et al. (2004). The luminosity was defined in the 0.013–13.6 keV band for each spectrum. Interestingly, the value of the ionisation parameter for obs 4 in Table 4 does not reflect the relative variations in the ionisation of the plasma with respect to obs 6–9 that we inferred in Sect. 4.1.1. The most likely reason for this is that the model that we are using as an ionising continuum for the photoionised absorber is not appropriate. If this is true, we expect to find the larger discrepancy between the ratio of Fe XXV and Fe XXVI lines and the ionisation parameter in obs 4, since this observation shows a column density for the ionised plasma larger by more than a factor of two compared to the other observations and this will cause severe obscuration of the continuum. Therefore, we re-fitted again all the spectra but using for all the observations the ionising continuum of obs 6. We chose obs 6 as the more realistic continuum since it has the most highly-ionised plasma and consequently more transparent to the incident radiation. We obtained $\log(\xi) = 4.18 \pm 0.15$, 4.39 ± 0.17 , $4.33^{+0.11}_{-0.15}$, $4.00^{+0.10}_{-0.19}$ and $4.09^{+0.11}_{-0.15} \text{ erg cm s}^{-1}$ for obs 4, 6–9, respectively. The other parameters and the quality of the fit did not change, as expected. These values are consistent with the line ratios of different species inferred from Table 3 and Fig. 4 and therefore we use these values rather than the ones in Table 4 in the remaining sections of this paper.

Finally, we note that obs 4, 8 and 9 show still after the fit small residuals at the energies of ~ 2.45 and 2.62 keV (see Fig. 7), that we identify with absorption from SXV and SXVI. Since we account for all the absorption features with the self-consistent model **warmabs**, the existence of residuals indicates that the abundance of Sulphur is most likely larger than the solar value. Another possibility would be the presence of a second absorber with a lower ionisation degree, but in this case, we should observe also residuals for other elements in the plasma. We did not attempt to fit the Sulphur abundances due to the small significance of the features, but we note that an overabundance of the S/Fe ratio with respect to the solar value was also pointed out by Ueda et al. (2004) based on *Chandra* HETGS data. They argued that this overabundance could indicate an underestimation of the column density of Fe due to the non-inclusion of reemission lines. Our data could be showing the same scenario, since we also observe small residuals at the energy of the Fe XXVI edge, which could disappear with an increase of the column density of Fe. Alternatively, the remaining residuals at the Fe XXVI edge in obs 4 and 9 could represent the limit of applicability of the **warmabs** model for high column densities (**warmabs** assumes a uniform ionisation for the absorber even if a large column density is present, which is not self-consistent). A small absorption feature remains also at $\sim 1.88 \text{ keV}$ in obs 8 and 9, which could be Si XIII, or systematic residuals at the Si edge due to a deficient CTI calibration (see Sect. 2).

4.1.3. Choice of continuum model

In previous section we showed that using the same ionising continuum for all the observations caused a significant change in the value of ξ for obs 4 and 9 and smaller, non-significant, changes in the other observations. From this, we infer that at least for obs 4 and 9 the continuum may not be unique. Continua that result in a similar quality of the fit in the 2–10 keV band may yield significantly different ionising continua when they are extrapolated to the 0.013–13.6 keV energy band.

There are several reasons for obtaining a “non-realistic” continuum in the limited XMM-Newton band-pass. First, different combinations of thermal and non-thermal components can be used for spectral fitting and the quality of the data does not usually allow to discriminate among them. Second, if the broad Fe line is caused by reprocessed emission, the “reprocessed” continuum should be also properly accounted for. A last possibility is that changes in the neutral and ionised absorber are mimicking a change of continuum, as it is the case in dipping sources (Boirin et al. 2005; Díaz Trigo et al. 2006). We examine these possibilities in detail below and in next section.

We substituted the continuum components of the fits reported in Table 4 by alternative non-thermal components. We found that the quality of the fits did not change. As an example, obs 6 had a χ^2_ν of 1.12 for

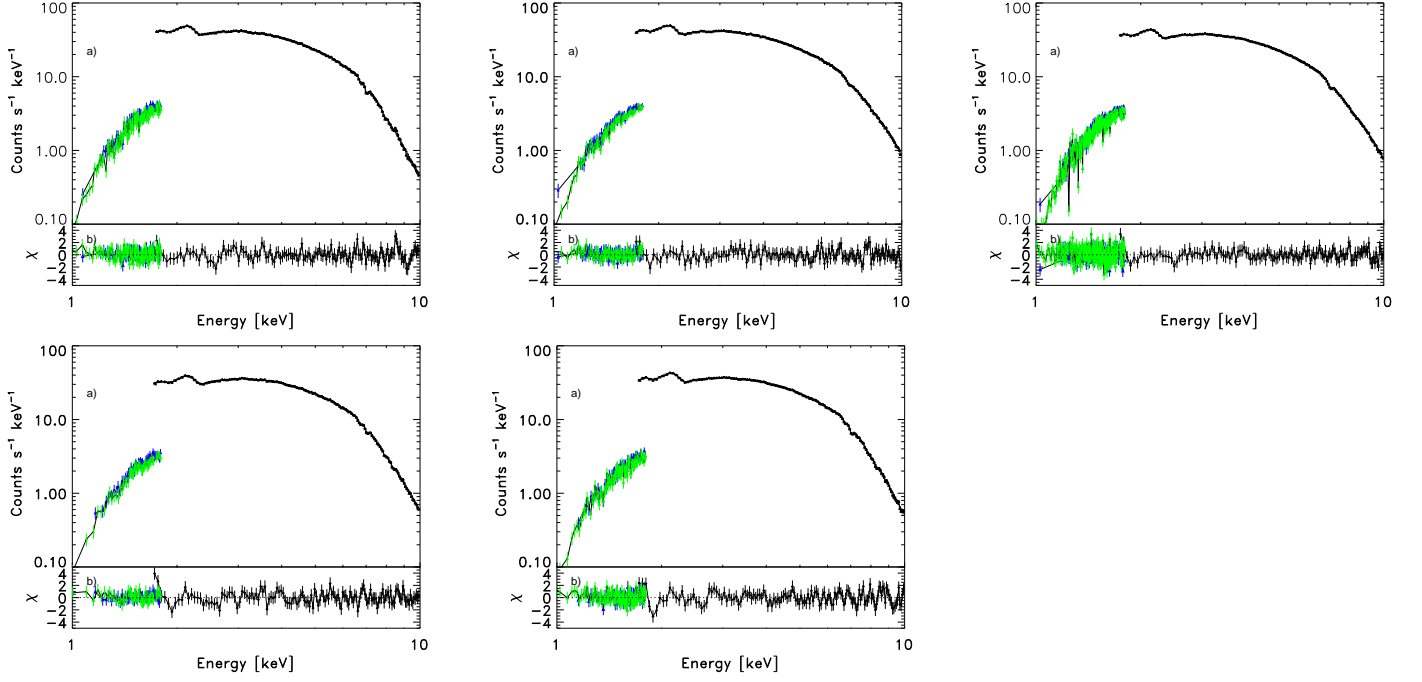


Fig. 7. Obs 4, 6 to 9 are shown from left to right and from up to bottom. (a) 1.7–10 keV EPIC pn (black), and 0.8–1.8 keV RGS1 (green) and RGS2 (blue) GX 13+1 spectra fitted with a disc-blackbody (`diskbb`), a black-body (`bbodyrad`) and a Gaussian (`gau`) components modified by absorption from neutral (`tbabs`) and ionised (`cabs*warmabs`) material. (b) Residuals in units of standard deviation from the above model.

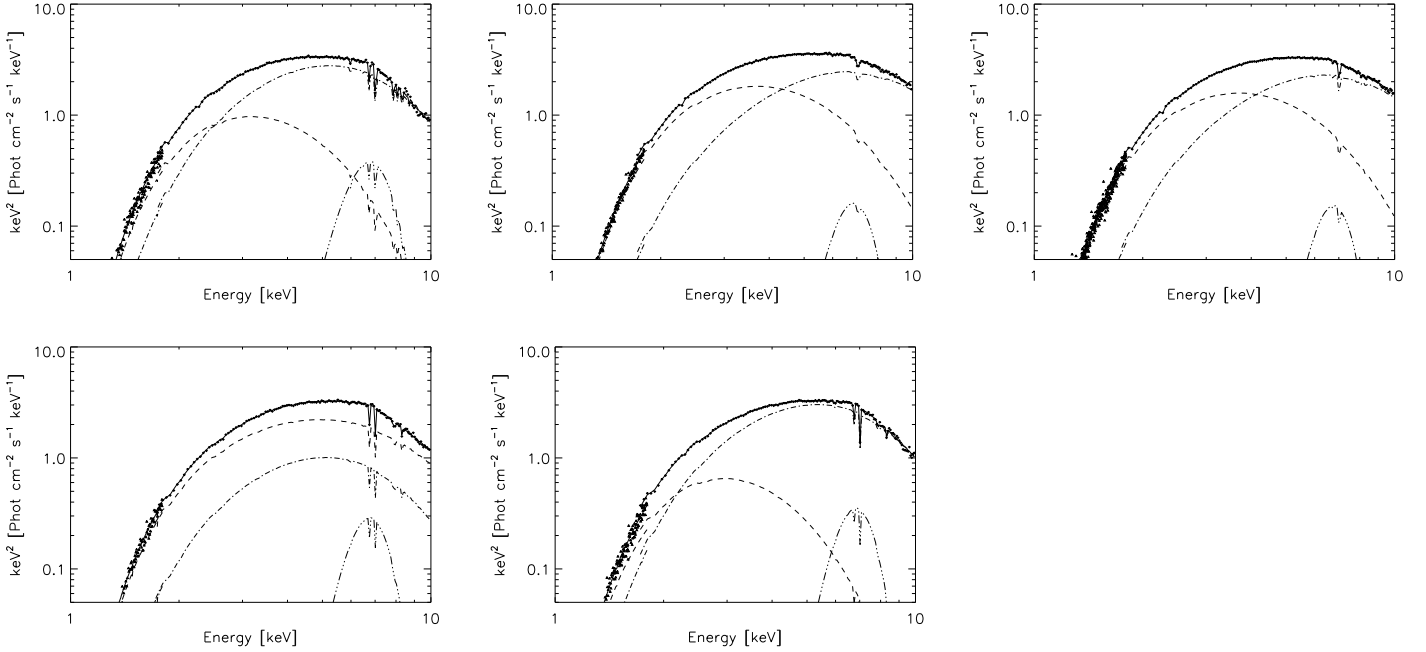


Fig. 8. 0.8–10 keV unfolded spectra. Solid, dashed, dot-dashed and dot-dot-dashed lines represent the contribution of the total model, disc, blackbody and Gaussian components, respectively.

701 d.o.f. when fitted with Model 2. Substituting the blackbody component by a power-law component in Model 2 (`tbabs*cabs*warmabs*(diskbb+po+gau)`, hereafter Model 3) we obtained $\chi^2_{\nu} = 1.12$ for 701 d.o.f.. The photon index, Γ , and normalisation of the power-

law were 2.2 ± 0.3 and 1.1 ± 0.4 , respectively, and the temperature and normalisation of the disc blackbody component $1.85^{+0.03}_{-0.06}$ keV and 46^{+8}_{-4} , respectively. Substituting the disc blackbody component by a power-law component in Model 2 (`tbabs*cabs*warmabs*(bbodyrad+po+gau)`,

Table 4. Best-fits to the 0.8–1.8 keV RGS and 1.7–10 keV EPIC pn persistent spectra for all the observations using the **tbabs*cabs*warmabs*(diskbb+bbrad+gau)** model. The column density of the **cabs** component was tied to the column density of the photo-ionised absorber (see text). k_{bb} , k_{dbb} and k_{gau} are the normalizations of the blackbody component, disc blackbody and Gaussian emission feature, respectively. kT_{bb} and kT_{dbb} are the temperatures of the blackbody and disc blackbody, respectively. E_{gau} and σ represent the energy and width of the Gaussian feature. $N_{\text{H}}^{\text{abs}}$ and $N_{\text{H}}^{\text{warmabs}}$ are the column densities for the neutral and ionised absorbers, respectively. ξ , σ_v , and v are the ionisation parameter (in units of erg cm s^{-1}), the turbulent velocity broadening, and the average systematic velocity shift of the absorber (negative values indicate blueshifts). F_{tot} is the unabsorbed total flux, and F_{gau} is the unabsorbed emission Gaussian flux. The width (σ) of the Gaussian emission line **gau** was constrained to be ≤ 1 keV in the fits.

Observation No.	4	6	7	8	9
Comp.					
Parameter					
dbb					
kT_{dbb} (keV)	$0.86^{+0.59}_{-0.07}$	$1.16^{+0.19}_{-0.07}$	$1.15^{+0.14}_{-0.08}$	$1.80^{+0.11}_{-0.14}$	$0.77^{+0.06}_{-0.04}$
$k_{\text{dbb}} [(R_{\text{in}}/D_{10})^2 \cos\theta]$	492^{+168}_{-369}	226^{+51}_{-54}	201^{+20}_{-44}	38 ± 8	622^{+188}_{-110}
bb					
kT_{bb} (keV)	1.24 ± 0.02	$1.66^{+0.24}_{-0.03}$	$1.60^{+0.08}_{-0.02}$	$1.21^{+0.08}_{-0.10}$	1.28 ± 0.01
$k_{\text{bb}} [(R_{\text{in}}/D_{10})^2]$	310^{+37}_{-154}	74^{+8}_{-35}	81^{+7}_{-31}	113^{+34}_{-38}	272^{+16}_{-21}
gau1					
E_{gau} (keV)	$6.56^{+0.10}_{-0.07}$	$6.71^{+0.12}_{-0.16}$	6.63 ± 0.11	$6.59^{+0.07}_{-0.15}$	6.69 ± 0.06
σ (keV)	$0.88^{+0.12}_{-0.07}$	$0.77^{+0.23}_{-0.15}$	$0.72^{+0.08}_{-0.12}$	$0.78^{+0.17}_{-0.09}$	$0.77^{+0.06}_{-0.08}$
$k_{\text{gau}} (10^{-4} \text{ ph cm}^{-2} \text{ s}^{-1})$	0.023 ± 0.006	$0.008^{+0.004}_{-0.002}$	$0.007^{+0.003}_{-0.001}$	$0.014^{+0.005}_{-0.003}$	0.017 ± 0.003
EW (eV)	299 ± 77	91^{+48}_{-23}	88^{+38}_{-13}	195^{+70}_{-42}	235 ± 42
tbabs					
$N_{\text{H}}^{\text{abs}} (10^{22} \text{ cm}^{-2})$	2.86 ± 0.05	2.86 ± 0.02	2.92 ± 0.02	2.77 ± 0.05	$2.87^{+0.06}_{-0.04}$
warmabs					
$N_{\text{H}}^{\text{warmabs}} (10^{22} \text{ cm}^{-2})$	$17.2^{+10.3}_{-6.8}$	$6.6^{+3.2}_{-2.7}$	$6.6^{+2.9}_{-0.4}$	$6.0^{+6.6}_{-2.0}$	$7.1^{+0.5}_{-2.3}$
$\log(\xi)$ (erg cm s^{-1})	$4.41^{+0.11}_{-0.19}$	4.39 ± 0.17	$4.34^{+0.22}_{-0.08}$	$3.97^{+0.19}_{-0.06}$	4.23 ± 0.10
σ_v (km s^{-1})	580^{+165}_{-75}	3390^{+1785}_{-2210}	2130^{+1220}_{-920}	480^{+490}_{-175}	975^{+970}_{-710}
v (km s^{-1})	-2310^{+420}_{-360}	-3690^{+300}_{-600}	-2160^{+270}_{-180}	-2130 ± 480	-2400 ± 360
$\chi^2_{\nu}(\text{d.o.f.})$	1.11 (586)	1.12 (701)	1.04 (686)	1.09 (548)	1.23 (575)
$F_{2-10 \text{ keV}}^{\text{tot}} (10^{-9} \text{ erg cm}^{-2} \text{ s}^{-1})$	9.6	9.5	8.7	8.0	8.3
$F_{2-10 \text{ keV}}^{\text{gau}} (10^{-11} \text{ erg cm}^{-2} \text{ s}^{-1})$	24.3	7.9	7.1	14.7	17.6
Exposure (ks)	5.2	8.9	13.5	6.5	6.7

hereafter Model 4) we obtained $\chi^2_{\nu} = 1.14$ for 701 d.o.f.. The photon index, Γ , and normalisation of the power-law were 2.27 ± 0.04 and 3.1 ± 0.2 , respectively, and the temperature and normalisation of the blackbody component 1.12 ± 0.02 keV and 281^{+4}_{-9} , respectively. We did not find significant changes in the parameters of the narrow features when using different continua. In contrast, the EW of the Gaussian component increased from 91^{+48}_{-23} eV in Model 2 to 201 ± 41 and 348^{+58}_{-16} eV in Models 3 and 4, respectively. Finally, substituting the power-law component in Models 3 or 4 by a cutoff or broken power-law components gave an unconstrained cutoff or break and a similar fit to the power-law.

We also obtained fits of the same quality when using different abundances. However, we obtained a change in the EW and breadth of the Gaussian component. As an example, in obs 6 the breadth and EW of the broad emission line increased from 91^{+48}_{-23} to 129^{+46}_{-21} eV when we

substituted the solar abundances of Anders & Grevesse (1989) by those of Wilms et al. (2000) in Model 2.

In summary, we found that the parameters of the warm absorber were stable to different choices of continuum components and abundances. In contrast, the parameters of the broad Fe line changed significantly, the main reason being that the quality of the fit before introducing the broad Fe line was worse for Models 3 and 4 than for Model 2.

4.1.4. Modeling of the broad Fe line and continuum variability

We examined the possibility that spectral changes between different observations are due to variations of the warm absorber and the reprocessed component instead of variations of the continuum. A motivation for this is Fig. 2. The resemblance of this figure with Fig. 4 of Boirin et al.

(2005) indicates that obs 8–9 (7) could be deep (shallow) dipping states with respect to obs 6 (see Sect. 3.1). If this is true we expect the continuum to be relatively stable and the dipping states to have a less ionised absorber and with a larger column density compared to the persistent ones (Borin et al. 2005; Díaz Trigo et al. 2006). Indeed, obs 8 and 9 show a less ionised absorber with visible features of Fe XXV, compared to obs 6 and 7. Similarly, obs 1–3 show a less ionised plasma than obs 4.

In order to test the continuum variability, we first substituted the Gaussian component by the **reflionx** model (Ross & Fabian 2005) to account for reflection by an ionised, optically thick, illuminated atmosphere of constant density. Since **reflionx** only provides the reflected emission, we added also a power-law component to account for the direct emission (**tbabs*cabs*warmabs*(diskbb+bodyrad+po+reflionx)**, hereafter Model 5), and we coupled the photon index of the illuminating power-law component to the index of **reflionx**. If the line is produced by reprocessed emission, Model 5 will yield a more realistic continuum, necessary to perform a simultaneous fit to several observations. We note that while **reflionx** is the most adequate of the available public models for our purposes since it includes self-consistently line emission and accounts for ionised reflection, more recent refined models such as those presented in García & Kallman (2010) point to important differences in the resultant spectrum when e.g. new atomic data are considered (see Sect. 5.2).

For the simultaneous fit we considered obs 6–9 only. We left out obs 4 since it is in a different track in Fig. 2, together with obs 1–3 and this may indicate already significant changes in the continuum (a significant increase in Compton scattering due to a larger column density of plasma could be also the reason for the different track of obs 1–4). We imposed the same continuum for obs 6–9 (including index and normalisation of the power-law component) and allowed only changes in the neutral absorber and the ionisation degree and normalisation of the reflection component. We kept the parameters of the warm absorber fixed to the values shown in Table 4 but with the values of the ionisation parameter obtained when the ionising continuum of obs 6 was used to fit all observations (see Sect. 4.1.2). Finally, we allowed a global difference in normalisation among observations to account for a potential different amount of Compton scattering.

We obtained a good quality for the simultaneous fit of obs 6–9 ($\chi^2_\nu = 1.21$ for 2537 d.o.f.). Table 5 shows the best-fit parameters and the residuals of the fit and unfolded spectra are shown in Fig. 9.

We could model the emission line with the reflection component and, as expected, the reprocessed component contributes significantly to the continuum emission. Thus, the interpretation of the continuum parameters should be done with caution. Interestingly, the large difference in the curvature of the spectrum at 7–10 keV between obs 6–7 and 8–9 can be well reproduced by a difference in the ionisation and normalisation of the reflected component.

In contrast, we were not able to reproduce the broad iron line with reflection models which consider a blackbody as an incident spectrum since they predict *EW*s that are too small compared to the observed lines.

Despite the success of Model 5 to reproduce the various spectral features of obs 6–9 while assuming a constant continuum, there are still some systematic residuals in the best-fit. The residuals at the absorption edge at the energy of Fe XXVI in obs 9 were already present in individual fits (see Sect. 4.1.2). However, the simultaneous fits show a slight curvature in the residuals which is not present in the individual fits and could be due to shortcomings of the reflection component, a different origin for the emission line, or an indication for continuum variability. Finally, if we attribute the differences in the global normalisation constant to Compton scattering of fully ionised plasma, the $\sim 30\%$ difference in normalisation between obs 6–7 and 8–9 implies that obs 6–7 are observed through an extra column density of $\gtrsim 10^{23} \text{ cm}^{-2}$ of fully ionised plasma.

4.2. RGS spectral analysis

We examined the 0.8–1.8 keV (9.9–22.3 Å) first order RGS spectra to constrain the N_{H} in the direction of the source and to search for the signature of narrow absorption and emission features. We note that the second order spectra have too few counts to add any value to the fits.

We could fit the RGS spectra of all the observations with a continuum consisting of a disc blackbody modified by photo-electric absorption from neutral material. We obtained a C-statistic of between 450 and 571 for ~ 434 –436 d.o.f. for obs 4 to 9). The values of N_{H} in units of 10^{22} cm^{-2} were 2.72 ± 0.06 , 2.73 ± 0.05 , $2.80^{+0.07}_{-0.03}$, 2.80 ± 0.06 , 2.76 ± 0.07 and $2.75^{+0.07}_{-0.05}$ for obs 4 to 9, respectively. None of the observations showed significant narrow features.

To evaluate the effect of the chosen continuum in the value of N_{H} , we substituted the disc blackbody by a power law. We obtained a C-statistic of between 448 and 570 for ~ 434 –436 d.o.f. for obs 4 to 9. The values of N_{H} in units of 10^{22} cm^{-2} were 2.53 ± 0.25 , 2.53 ± 0.19 , 2.80 ± 0.19 , 2.71 ± 0.20 , 2.41 ± 0.26 and $2.16^{+0.22}_{-0.16}$ for obs 4 to 9, respectively.

Finally, to evaluate the effect of the absorption component in our fit, we substituted the **tbabs** component by the more recent **tbnew** component and re-fitted the combined spectra. The C-statistic and values of N_{H} did not change.

In summary, we obtained consistent values of N_{H} for different models of interstellar absorption but significantly different values of N_{H} when using different continuum components. This is expected due to the combination of limited energy band of the RGS and low statistics of these observations. Therefore, we conclude that the RGS spectra alone cannot constrain the value of N_{H} for these observations due to the poor statistics and the limited bandwidth, necessary to determine the continuum.

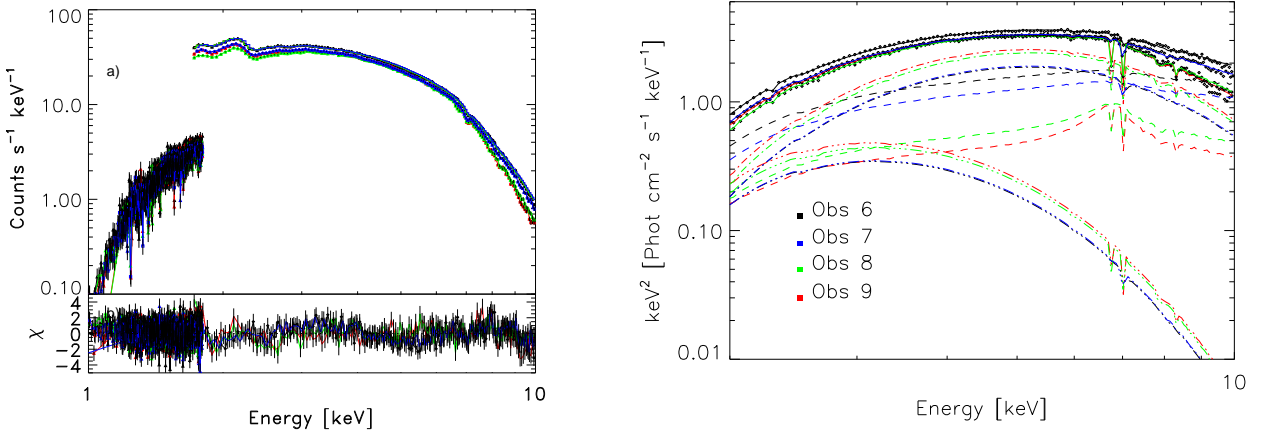


Fig. 9. *Left:* (a) 1.7–10 keV EPIC pn, and 0.8–1.8 keV RGS1 and RGS2 GX 13+1 spectra fitted with Model 5 (see text). (b) Residuals in units of standard deviation from the above model. *Right:* 1–10 keV unfolded spectra. Solid, dot-dot-dashed and dot-dashed lines represent the contribution of the total model, disc, blackbody and reflection components, respectively. Obs 6–9 are shown in black, blue, green and red, respectively.

Table 5. Best-fits to the 0.8–1.8 keV RGS and 1.7–10 keV EPIC pn persistent spectra for all the observations using the `const*tbabs*cabs*warmabs*(diskbb+bbrad+po+reflionx)` model (see caption of Table 4 for definitions). Γ is the index of the incident power-law and is coupled to the index of `reflionx`. k_{po} is the normalisation of the power-law component and ξ and $k_{reflionx}$ are the ionisation parameter and the normalisation of the reflection component. The parameters of `warmabs` and `cabs` have been fixed to the values of Table 4.

Observation No.	6	7	8	9
Parameter	Comp.			
kT_{dbb} (keV)	dbb			
$k_{\text{dbb}} [(R_{\text{in}}/D_{10})^2 \cos\theta]$	$0.86^{+0.08}_{-0.06}$			
kT_{bb} (keV)	bb			
$k_{\text{bb}} [(R_{\text{in}}/D_{10})^2]$	$1.23^{+0.01}_{-0.04}$			
Γ	po			
k_{po} (ph keV $^{-1}$ cm $^{-2}$ s $^{-1}$ at 1 keV)	1.94 ± 0.02			
$\log(\xi)$ (erg cm s $^{-1}$)	reflionx			
$k_{reflionx}$ (10 $^{-6}$)	$3.94^{+0.06}_{-0.17}$	$3.83^{+0.05}_{-0.08}$	3.41 ± 0.04	$3.30^{+0.01}_{-0.04}$
$N_{\text{H}}^{\text{abs}}$ (10 22 cm $^{-2}$)	tbabs			
$Const$	const			
$\chi^2_{\nu}(\text{d.o.f.})$	1 (f)	1.02 ± 0.03	1.29 ± 0.03	$1.37^{+0.02}_{-0.05}$
	1.21 (2537)			

In order to increase the sensitivity to narrow lines and edges, we combined the RGS spectra of several observations. We added the RGS1 and RGS2 spectra of obs 4, 8 and 9 (set 1) and separately of obs 5, 6 and 7 (set 2). The reason to distinguish between sets is that the former set of observations shows possible “obscuration” events (see Sect. 4) and, if confirmed, such events indicate

a plasma with lower ionisation degree than the second set of observations. We could fit the resultant spectra with the same model as the individual observations. We obtained a C-statistic(d.o.f.) of 318(280) and 390(280) and $N_{\text{H}}=2.74 \pm 0.04$ and $2.78^{+0.02}_{-0.04} \times 10^{22}$ cm $^{-2}$ for sets 1 and 2, respectively, when using a disc blackbody continuum

and of 292(280) and 385(280) and $N_{\text{H}}=2.33\pm0.15$ and $2.67\pm0.11\times10^{22}\text{ cm}^{-2}$ when using a power law.

None of the merged data sets shows any additional narrow features and including absorption from a photo-ionised plasma in the model does not improve the fit quality. We calculated upper limits for the existence of the Mg XII absorption feature detected in the *Chandra* observation with an EW of 2 eV (Ueda et al. 2004). Assuming that the feature is narrow (width fixed to 0), we obtained upper limits to the EW between 1 and 3 eV for obs 4–8 for a feature with no velocity shift. For obs 9 we obtain a non-significant detection of an absorption feature with $EW=2.5^{+2.1}_{-2.2}$ eV. Then, we assumed velocity blueshifts up to 4000 km/s in steps of 500 km/s and calculated upper limits at the corresponding wavelengths. We obtained upper limits to the EW between 0.5 and 4.2 eV for obs 4, 7–9. For obs 6 we obtain a non-significant detection of an absorption feature at a blueshift of 2000 km/s with an $EW=2.0^{+1.5}_{-1.6}$ eV. These results are consistent with the predicted EW for Mg XII, $\lesssim 1$ eV, for an ionised absorber of $\log \xi \gtrsim 4$, as fitted in the EPIC pn exposures.

4.3. OM data

We extracted images and light curves from the U, UVW1 and UVM2 filter OM exposures for obs 4–9.

The images show a source in the U filter exposures consistent with the position of GX 13+1, which is strongest in obs 4 and weakest in obs 7. The source was not detected in the UVW1 or UVM2 filters, except for obs 5 where there is a detection with the UVW1 filter with a magnitude of 20.7 ± 0.7 . For obs 4, 5, 7 and 8 we obtained average U optical magnitudes of 19.8 ± 0.4 , 19.7 ± 0.2 , 20.8 ± 0.7 and 20.5 ± 0.5 , respectively. We note that GX 13+1 is not detected in the U exposures in obs 6 and 9.

Obs 4 showed a significant variation in the U magnitude with time, from 20.4 ± 0.4 to 19.2 ± 0.1 within a 9 ks interval. Unfortunately, we cannot determine the presence of a modulation with orbital phase due to the few detections of the source. Therefore we do not use the OM data any further.

5. Discussion

We analysed five XMM-Newton observations of the LMXB GX 13+1 taken during 2008 to investigate the variability and origin of the disc wind present in this source.

The 0.6–10 keV EPIC pn lightcurves were highly variable with two observations showing energy-dependent obscuration, similar to the classical dipping sources.

The X-ray continua of the “least variable” intervals were well fitted by a model consisting of a blackbody and disc-blackbody components absorbed by neutral and ionised material. We could substitute the blackbody or disc-blackbody components by a non-thermal component such as a (cutoff) power-law or a Comptonisation component without significantly worsening the quality of the

fit. However, we found a significant change in the parameters of the broad emission line when such non-thermal components were used (see Sect. 4.1 and 5.2).

Lin et al. (2007) showed that the commonly used models for thermal emission plus Comptonisation were not favoured for the “Soft State” of two atoll sources because they failed to satisfy various desirability criteria, such as the $L_X \propto T^4$ evolution for the multi-colour disc blackbody component and similarity to black holes for correlated timing/spectral behaviour. Similarly, in a systematic analysis of 16 NS LMXBs observed with XMM-Newton, Ng et al. (2010) found that a continuum consisting of a disc blackbody and blackbody components was favoured in 80% of the cases. In this model, the blackbody component was interpreted as emission from a radiation pressure supported boundary layer. The data analysed in this work give further support to a continuum with two thermal components. However, we note that since XMM-Newton effective area is already very low at ~ 10 keV, we cannot decide based on this data whether an additional power-law component extending to high energies, like the one detected by INTEGRAL up to ~ 40 keV (Paizis et al. 2006), would be requested above 10 keV. If confirmed, the presence of a reprocessed component representing reflection by an ionised, optically thick, atmosphere illuminated by a power-law component (see Sect. 4.1.4) gives indirect evidence of the existence of a power-law component extending to high energies.

Ueda et al. (2004) used a blackbody and disc blackbody to fit the 3–25 keV RXTE/PCA spectrum of GX 13+1 and obtained a satisfactory fit but the values for the temperatures of the disc and blackbody components were significantly different than those reported in Table 4. Taking into account the flux and the ionisation of the disc wind, the RXTE/PCA observation should be in a similar state to obs 7. However, Ueda et al. (2004) report a temperature of 1.52 ± 0.03 keV and of 2.56 ± 0.02 keV for the disc and blackbody components, much larger than the ones found in this work for obs 7. Clearly, the absolute parameters of the continuum should be taken with caution in fits with limited energy band coverage.

5.1. Photoionised absorption

Absorption from highly-ionised species was present in all the observations of GX 13+1 analysed in this work.

An absorption feature consistent with Fe XXVI was first discovered by ASCA (Ueda et al. 2001). XMM-Newton observations in 2000 (obs 1–3) showed a complex of absorption lines and edges consistent with absorption from Ca XX, Fe XXV and Fe XXVI (Sidoli et al. 2002), similar to the complex found in obs 4, 8 and 9. Ueda et al. (2004) found additional features of S XVI, Si XIV, Mg XII, Mn XXV, Cr XXIV and Ar XVII in a posterior *Chandra* HETGS observation in 2004 and measured a blueshift of ~ 400 km and an ionisation parameter of $\log(\xi) \sim 4.1$ –4.7 for the plasma responsible for the absorption. A plasma density

$\gtrsim 10^{13} \text{ cm}^{-3}$ and a launching radius for the wind of $\sim 10^{10}$ – 10^{11} cm was inferred.

The depth of the absorption features in the XMM-Newton 2008 observations changed significantly in timescales of few days, and more subtle variations are seen in shorter, hours, timescales (Sidoli et al. 2002).

We found column densities for the absorber between 6 and $17 \times 10^{22} \text{ cm}^{-2}$ and ionisation parameters, $\log(\xi)$, between 4 and 4.4 erg cm s^{-1} . Obs 4 shows a column density larger by more than a factor of two with respect to the other observations, and which is poorly constrained. This, and the well constrained velocity indicate that the lines lie in the saturated region of the curve of growth, where the EWs of the lines do not depend on the column density anymore but increase with the velocity broadening. We observed a correlation between the ionisation parameter and the turbulent velocity of the warm absorber (see Fig. 10).

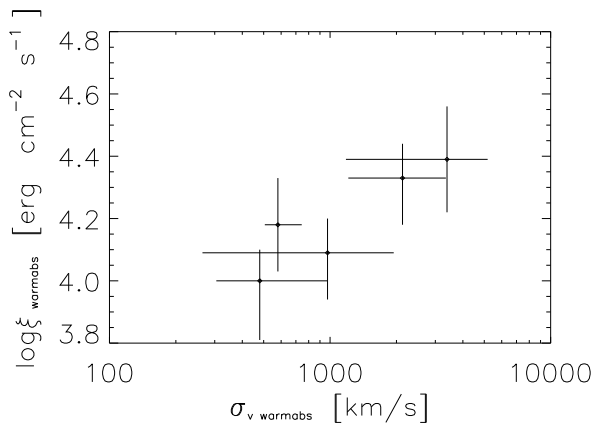


Fig. 10. Ionisation parameter of the warm absorber with respect to its turbulent velocity.

We found blueshifts between ~ 2100 and 3700 km s^{-1} for obs 4–9. Such blueshifts seem too large, compared to the shifts of $\sim 400 \text{ km s}^{-1}$ obtained by Ueda et al. (2004) for GX 13+1 and of ~ 300 – 1600 km s^{-1} in microquasars (e.g. Kallman et al. 2009; Ueda et al. 2009, see however Miller et al. (2011) for a recently reported blueshift of $3100 \pm 400 \text{ km/s}$ in a *Chandra* HETGS observation of IGR J17480–2446). Unfortunately, we do not detect any discrete absorption features from the warm absorber in the RGS, which has a much better energy resolution than EPIC. The lack of spectral features in the RGS wavelength range is consistent with the high degree of ionisation of the absorber (see Sect. 4.2). Thus, a more accurate measurement of the blueshifts is not possible for these observations. However, it seems plausible that the shifts detected with the pn camera are overestimated compared to the real blueshifts due to residual calibration uncertainties (see Sect. 4.1.1).

We can calculate the distance between the ionising source and the slab, r . Since $\xi = L/n_e r^2$ and $n_e \sim$

$N_{\text{H}}^{\text{warmabs}}/d$ (where d represents the thickness of the slab of ionised absorbing material), we can calculate r as $(L/\xi N_{\text{H}}^{\text{warmabs}})(d/r)$. Considering plausible values of d/r range between 0.1 and 1, we obtain values of r between $3 \times 10^9 \text{ cm}$ and $1 \times 10^{11} \text{ cm}$. Further, assuming that the value of r should not change significantly between observations, we estimate r as 1 – $3 \times 10^{10} \text{ cm}$, in excellent agreement with the value obtained by Ueda et al. (2004) of $2 \times 10^{10} \text{ cm}$.

The characteristics of the wind allow us to discriminate among the possible launching mechanisms, namely thermal, radiative, magnetic or a combination of them. Thermal driving is effective at large distances from the central compact object, black hole or NS, where the thermal velocity exceeds the local escape velocity. Thermally driven models are thus most effective in producing slow winds and at large radii. The distance at which the wind is launched in GX 13+1, 1 – $3 \times 10^{10} \text{ cm}$, points to a thermal origin, as discussed by Ueda et al. (2004). Moreover, the fact that the only known NS LMXBs showing winds are GX 13+1 (Ueda et al. 2004) and IGR J17480–2446 (Miller et al. 2011) is a logical consequence of the wind launching mechanism being thermal. As X-rays heat low density gas to a temperature $T \sim 10^7 \text{ K}$, the surface of a heated disc is expected to either puff up and form a static corona or emit a thermal wind, depending whether the thermal velocity exceeds the local escape velocity (Begelman et al. 1983; Woods et al. 1996; Proga & Kallman 2002). Woods et al. (1996) estimated that for a radius of $\sim 2.6 \times 10^{10} \text{ cm}$, an isothermal wind would develop for luminosities above $\sim 3 \times 10^{37} \text{ erg s}^{-1}$, while such a wind would be inhibited by gravity at lower luminosities (see their Fig. 17). For larger radii, a steadily heated free wind could develop already at luminosities below $\sim 3 \times 10^{37} \text{ erg s}^{-1}$. Proga & Kallman (2002) found that including the radiation force due to electron scattering, the radius at which the maximum of mass flux density occurred could be reduced by a factor of 20 compared to the calculations of Woods et al. (1996). Taking these values into account, the luminosity, and not the radius, seems to be the critical parameter for the existence of a wind in the classical dipping sources. Indeed, all the dipping sources showing ionised absorption for which no significant blueshifts have been detected (Cottam et al. 2001; Sidoli et al. 2001; Juett & Chakrabarty 2006; Boirin et al. 2005; Iaria et al. 2007) have a luminosity below the one needed for the wind to overcome gravity in these models (see Table 1 of Díaz Trigo et al. 2006), with the possible exception of MXB 1658–298, which has a luminosity close to the critical value. In contrast, X 1624–490, GX 13+1 and IGR J17480–2446 have luminosities of 4.7×10^{37} , 6 – 9×10^{37} and $3.7 \times 10^{37} \text{ erg/s}$, respectively, close to or above the critical luminosity. From these sources, two show clearly outflowing winds (see above) and the third one, X 1624–490, shows a significant blueshift of $607^{+354}_{-342} \text{ km/s}$ for the most highly ionised absorbing component in *Chandra* HETGS observations (Xiang et al. 2009). In summary, a thermal wind launching mechanism

can explain the appearance of hot static atmospheres or slow disc winds in all high inclination NS LMXBs and its absence in low inclination NS LMXBs. We caution that Compton scattering in a hot atmosphere or disc wind with column densities above 10^{22} cm^{-2} can reduce significantly the flux of the central source seen by a distant observer. Therefore, a potential larger luminosity than “observed” (as the luminosity of the system could be significantly underestimated due to Compton scattering) and the radiation force due to electron scattering when a large column density of highly ionised plasma is present, should be always considered before ruling out the thermal wind launching mechanism.

Finally, if the thermal wind launching mechanism is in place for all NS LMXBs, we expect that a disc wind will develop for systems brighter than GX 13+1, known as Z-sources, since their luminosity is well above the critical luminosity. Ueda et al. (2004) estimated the mass outflow rate in GX 13+1 to be $\gtrsim 0.7\text{--}2.7 \times 10^{18} \text{ g s}^{-1}$. They assumed that the plasma had an equatorial geometry and was outflowing from both sides of the disc to define a solid angle of $\Omega/4\pi = 0.4$. In our observations, taking a similar solid angle into account we calculate outflow rates of $0.1\text{--}0.2 \times 10^{18} \text{ g s}^{-1}$ for an outflow velocity of 400 km s^{-1} , as found by Ueda et al. (2004), and of $0.5\text{--}1 \times 10^{18} \text{ g s}^{-1}$ for an outflow velocity of $2000\text{--}3500 \text{ km s}^{-1}$, as found in these observations. This outflow rate is comparable with the mass accretion rate of 10^{18} g s^{-1} , as already pointed out by Ueda et al. (2004), and implies that the disc wind could play an important role in the whole dynamics of the accretion disc for such bright sources. Proga & Kallman (2002) calculated the mass-outflow rate for a NS accreting at a rate of $1.3 \times 10^{18} \text{ g/s}$ and found mass-outflow rates between 3.9×10^{15} and $0.65 \times 10^{18} \text{ g/s}$ for different values of X-ray attenuation (see their Table 1). Unfortunately, from their simulations we cannot estimate what is the effect of increasing the mass accretion rate in the mass-outflow rate for a given value of X-ray attenuation. However, the fact that for the same attenuation, an increase in accretion rate results in an increase of column density of the ionised plasma (see e.g. models L2 and H2 in their Table 1) may indicate that the mass-loss rate will be larger for sources with higher accretion rate, since the radiation pressure due to electron scattering will also increase for such sources.

Although narrow absorption features are not detected in the Z-sources, most likely due to a lower inclination or to fully ionised winds, if we consider other signatures of a disc wind such as broad iron line emission (see Sect. 5.3) a study of the strength of the wind in such sources may become possible and of utmost importance to evaluate the balance between inflowing and outflowing matter in such systems.

5.2. Broad iron line emission

We found a broad, $\sigma \sim 0.7\text{--}0.9 \text{ keV}$, emission line in all the observations analysed in this work. The energy centroid

varied between 6.55 and 6.7 keV, consistent with emission of highly ionised species of iron (Fe XXI–Fe XXV). The *EW* of the line increased from $\sim 100 \text{ eV}$ in obs 6 and 7 to $\sim 300 \text{ eV}$ in obs 4.

The absolute breadth and *EW* of the lines was strongly dependent on the continuum model. As an example, the *EW* of the line in obs 6 increased from 91_{-23}^{+48} to 201 ± 41 (348_{-16}^{+58}) eV when we substituted the disc blackbody (blackbody) component by a power-law component in Model 2 (see Sect. 4.1.2). For this highly absorbed source we also found a dependency of the breadth and *EW* of the line on the abundances used, which caused a significant change in the continuum parameters, especially in the soft band. For obs 6, we obtained an *EW* of 91_{-23}^{+48} eV using solar abundances from Anders & Grevesse (1989) and of 129_{-21}^{+46} eV with abundances from Wilms et al. (2000). In general, continuum models that yielded a higher χ^2_ν for the fit before adding the line resulted in broader lines, since the Gaussian component absorbed the deficiencies of the continuum model. Hence, it is challenging to investigate the origin of the broad iron line based on its absolute parameters. In contrast, we can examine the relative changes of the line among observations, since any systematic effect caused by our choice of continuum, abundances or spectral analysis should be the same for all observations. Further, since we are comparing observations of one source and taken with the same instrument, residual calibration effects or properties of the source such as inclination should not affect our conclusions.

The presence of broad Fe lines in NS LMXBs has been extensively studied (see White et al. 1986; Hirano et al. 1987; Asai et al. 2000; Ng et al. 2010, for systematic studies with different X-ray observatories). In these systems, broad lines could arise in the inner accretion disc by fluorescence following illumination by an external source of X-rays (e.g. the boundary layer where the accretion disc meets the star), and be broadened by relativistic effects near the compact object (e.g. Reynolds & Nowak 2003; Fabian & Miniutti 2005; Matt 2006). Alternatively, they could originate in the inner part of the so-called accretion disc corona, formed by evaporation of the outer layers of the disc illuminated by the emission of the central object (e.g., White & Holt 1982; Kallman & White 1989) and be broadened predominantly by Compton scattering (e.g. Pozdnyakov et al. 1979; Sunyaev & Titarchuk 1980). A third possibility, is that they originate in a partially ionised wind as a result of illumination by the central source continuum photons and are broadened by electron downscattering in the wind environment (Laurent & Titarchuk 2007). The first interpretation differs from the other two in that Compton scattering does not suffice to broaden the lines to the observed values, hence relativistic broadening has to be invoked. Therefore, to discriminate between the different interpretations it is key to determine the characteristics of the plasma where the lines originate, mainly its temperature and state of ionisation, by comparison with detailed reflection models.

Recently, García & Kallman (2010) presented new models for illuminated accretion discs and their structure implementing state-of-the-art atomic data for the isonuclear sequences of iron and oxygen and increasing the energy, spatial and angular resolution compared to previous works. They found *EW*s of the Fe K emission line between 400 and 800 eV for the cases with $\log(\xi)$ between 1 and 3. The line *EW*s decreased rapidly for higher values of ξ , with $EW \sim 40$ eV for $\log(\xi) = 3.8$. The *EW*s of the lines found in this work range between ~ 90 and ~ 300 eV, indicating a plasma with $\log(\xi)$ between ~ 3.7 and 3^6 (see also Fig. 2 of García et al. 2011), in broad agreement with the values of $\log(\xi) \sim 3.3$ – 3.9 found for the reflection component used to model the emission line in Sect. 4.1.4. For these values of the ionisation parameter García et al. (2011) found that the most prominent lines had centroids between 6.65 and 6.74 keV, slightly larger than the values found in this work, 6.56–6.71 keV, but still consistent within the errors.

In summary, we found that the lines observed in this work can be explained by ionised reflection of the disc. In this model, the breadth of the lines results primarily from the Compton scattering in the hot atmosphere or corona, and relativistic effects are not required as a broadening mechanism.

However, the contemporaneous evolution of warm absorption and broad Fe line emission for the observations analysed in this work indicates that they probably form in the same environment, namely the disc wind (see sect. 5.3). As pointed out by Sim et al. (2010a), in the presence of a disc wind we expect a scattered/reprocessed component that is qualitatively similar to that produced by standard disc reflection models. In particular, a moderately strong Fe line is present in both models. In contrast, it is difficult to justify the contemporaneous changes of the broad iron line and the absorption features if the former is produced at the inner disc or the boundary layer, as expected in the classical reflection scenarios, and the latter at the outer disc, as shown in Sect. 5.1. We note that strong broad Fe lines were predicted for LMXBs which had a wind with a Thomson scattering optical depth close to unity far from the compact object and which is illuminated by a hard component (Laming & Titarchuk 2004). In that model, the optical depth in the Fe K continuum is about 1–3 times higher than that due to electron scattering. The wind found in obs 4, for which the Fe line is strongest, has a column density of $2 \times 10^{23} \text{ cm}^{-2}$, but this may be only a lower limit to the real column density. The fact that the absorption lines are saturated and that the absorption edges are not properly fitted points to a failure of the **warmabs** model when the optically thick limit is approached. Therefore the conditions necessary for a wind origin of the broad line are most likely fulfilled.

Finally, while we cannot assure that a hard illuminating component, as the one assumed by Laming & Titarchuk (2004), is present in this data due to the limited energy coverage of XMM-Newton, if such component is absent, disc reflection would not be an alternative mechanism, since strong lines cannot be produced with a soft illuminating component (see Fig. 3 of Ballantyne 2004).

Therefore, we favour reprocessing in a hot atmosphere or disc wind as the origin for the broad Fe line in NS LMXBs and justify this in detail in next section.

5.3. A disc wind as a self-consistent scenario for photoionised absorption and broad iron line emission

Neilsen & Lee (2009) reported the presence of a broad emission line in the faint, hard states and narrow absorption lines in the bright, soft states of the microquasar GRS 1915+105. Since the hard states exhibit prominent radio jets, which are absent during the soft states, they argued that the broad emission line arises when the jet illuminates the inner accretion disc and the absorption lines originate when the powerful radiation field around the black hole drives a hot wind off the accretion disc. Since GX 13+1 shows also jets, which are associated with hard states (Grindlay & Seaquist 1986), we could expect a similar behaviour regarding the appearance of broad emission lines and narrow absorption lines as for GRS 1915+105.

In contrast, we observe contemporaneously broad emission line and narrow absorption lines similarly to most of the classical dippers, and the emission line becomes stronger as the hard flux decreases. Moreover, we find that the *EW* and the width of the broad Fe line increase with the column density of the absorber (see Fig. 11, upper panels), a decrease of the *EW* of the broad line with the increase of the ionisation parameter of the absorber (Fig. 11, lower-left panel) and a simultaneous increase in the ionisation of the absorber and the energy centroid of the broad line (Fig. 11, lower-right panel). We can naturally explain all these correlations in the frame of a disc wind scenario in which both the absorption and the emission are produced in the wind (Laurent & Titarchuk 2007; Sim et al. 2010a). In this scenario, we observe absorption features as we look through the wind (predominantly in high inclination sources), while the radiation scattered in the outflow produces the broad iron line emission and other distinct features such as a Compton hump, which will be more or less visible depending on their contribution with respect to the incident radiation. Higher column densities make scattered/reprocessed radiation more dominant and so we observe a most prominent iron line whenever the column density of the absorbing plasma is larger and the ionisation smaller. We refer to Sim et al. (2010a,b) for a detailed explanation of the total spectra expected at different inclinations and for different characteristics of the wind and summarise the relevant results in what follows.

⁶ We note that these values of $\log(\xi)$ cannot be directly compared with those of the warm absorber, since the models shown in García & Kallman (2010) have an ionising continuum consistent of a power law with index 2.

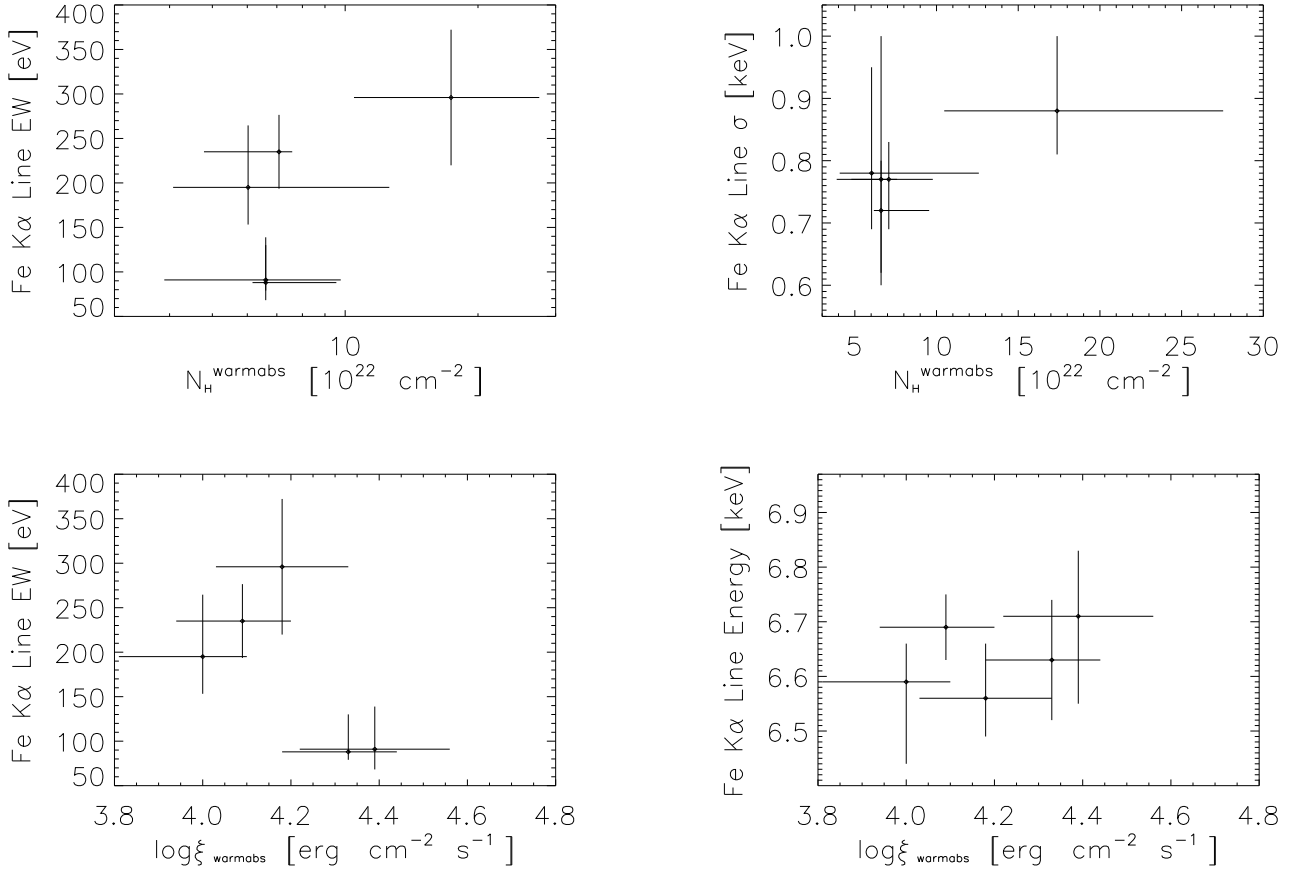


Fig. 11. *Upper panels:* EW (upper-left) and width (upper-right) of the broad iron line with respect to the column density of the warm absorber. *Lower panels:* EW (lower-left) and energy (lower-right) of the broad iron line with respect to the ionisation of the warm absorber.

At low, $\lesssim 45^\circ$, inclinations the wind does not obscure the X-ray source. However, a significant component of scattered/reprocessed radiation in the outflow is present in addition to the direct emission and responsible for the broad iron line emission. The emission is predominantly formed by Fe XXV and Fe XXVI, since the part of the wind seen at low inclinations is the inner, highly ionised, surface of the outflow. Sim et al. (2010b) report emission features that are moderately strong, ~ 140 eV in their example, and which are significantly broadened by the Doppler motions of the material to a width of $\sigma \sim 0.3$ keV. This is consistent with what Ng et al. (2010) report in a systematic study of low-inclination (non-dipping) NS LMXBs with XMM-Newton. First, they report an emission line for 80% of the sources, i.e. the line is almost ubiquitous. Second, they report a weighted average energy for the sample of 6.67 ± 0.02 keV, consistent with Fe XXV, and a width of $\sigma = 0.33 \pm 0.02$ keV. Finally they find EWs between 17 and 189 eV. Indeed, a qualitative comparison of Fig. 4 of Sim et al. (2010a) with Fig. 3 of Ng et al. (2010) indicates that even the shape of the lines looks similar. In particular, the line of 4U 1705-44 shown in Fig. 3 (third row, third column) of Ng et al. (2010) is strikingly similar to

the one shown in Fig. 4 (upper-left panel) of Sim et al. (2010a).

As the inclination increases to $\sim 60^\circ$, the hottest and most ionised layers of the outflow are first intercepted. At this inclination the material is almost fully ionised and the only important opacity source is Compton scattering. Due to the energy dependence of the relativistic Klein-Nishina formula for Compton scattering, the opacity will be lower and the spectrum will curve upwards at high energies. Compared to lower inclinations, the emission feature will be slightly broader since a larger column density and gradient in velocity fields will be traversed. Sim et al. (2010b) report widths of around 0.35 keV and appearance of blueshifted Fe XXVI narrow absorption lines. At even higher inclinations, the part of the wind seen by the observer is less ionised and has a larger column density, and consequently the absorption features of less ionised ions, such as Fe XXV, become deeper. The direct component of the spectrum becomes increasingly dominated by the scattered/reprocessed component resulting in a prominent emission lines with EWs of up to 400 eV (Sim et al. 2010b). This is consistent with the results of this work and of previous works on classical dippers (i.e. high inclination

sources), in which narrow absorption lines and broad iron lines are observed simultaneously (e.g. Sidoli et al. 2001; Parmar et al. 2002; Boirin et al. 2005; Díaz Trigo et al. 2009). Boirin et al. (2005) and Díaz Trigo et al. (2006) found that a highly ionised absorption plasma is ubiquitous for these sources and inferred that such an equatorial plasma must be present in all LMXBs. Since the plasma will develop as a wind or not depending on the size of the system and on its luminosity (see Sect. 5.1), in cases where the thermal wind cannot develop due to the low luminosity of the central source the scattering will be produced in the hot, static, atmosphere that is revealed through absorption lines.

A caveat of the scenario outlined above may be the relevance of radiation pressure in the disc wind. Sim et al. (2010a,b) considered parameters typical of AGN for the disc wind simulations, for which radiation pressure and line-driving is considered to be more important than for LMXBs (see e.g. Proga & Kallman 2002). For example, the inner launching radius is expected to be smaller for AGN and the blueshifts of the absorption lines larger. However, the large column density of the absorber in obs 4 indicates that electron scattering and therefore radiation pressure is non-negligible and that shielding could be even relevant for some parts of the wind. An extrapolation of the region of emission line formation found by Sim et al. (2010b) of $4.7 \times 10^3 r_g$ to GX 13+1 yields a radius of $\sim 10^9$ cm, very close to the estimated launching radius of the wind of $\sim 10^{10}$ cm. Therefore, dedicated simulations for disc winds with parameters appropriate to LMXBs are now of utmost importance to allow spectral modeling and confirm this scenario.

5.4. Orbital period dependence of the wind

We found significant variability both within each observation and among all the observations analysed in this work. If the disc wind scenario outlined in the previous section is correct, we can naturally explain the spectral differences as different parts of the wind being probed at different phases, i.e. changes in the column density and ionisation of the warm absorber/wind in the line of sight and of the reprocessed component drive the spectral variability among observations.

Corbet et al. (2010) reported a modulation of ~ 24 d based on RXTE/ASM data spanning 14.2 years. They also found that the modulation is not constant. For example, their Fig. 6 indicates that for some time intervals the dominant peak is ~ 24 d but for others the peak lies below (third panel from the bottom) or above (second panel from the bottom). The fact that a modulation is observed in X-rays (Corbet et al. 2010) indicates most likely a high inclination for the source. Although regular dipping has not been reported for GX 13+1, this could be due to the long orbital period of ~ 24 d and the lack of a precise ephemeris. While modulation in NIR can be explained e.g. by a modulation of the companion (but note

that Froning et al. (2008) attribute 3/4 of the NIR flux to the disc), it is difficult to explain a periodicity in X-rays without invoking structure in the accretion disc or its atmosphere. Further, the detection of drops of intensity of up to 80% in the light curves of GX 13+1 which are energy-dependent strongly resembles the so-called dipping behaviour of high-inclination sources (see e.g. Fig. 1 of Díaz Trigo et al. 2006). Therefore, interpretations of the spectral/timing behaviour of the source in the context of Doppler boosting of a jet pointing directly towards us (Schnerr et al. 2003) are very unlikely at the light of the 2008 XMM-Newton observations. Instead we favour an inclination for the system of $\sim 60-80^\circ$.

Corbet et al. (2010) concluded that the X-ray modulation could be caused by dipping behaviour and that the structure causing the modulation should not be phase-locked. In classical dippers, the dips recur at the orbital period of the system and are believed to be caused by periodic obscuration of a central X-ray source by structure located in the outer regions of a disc resulting from the impact of the accretion flow from the companion star into the disc (White & Swank 1982). However, the structure is locked at phase ~ 0.8 (considering phase 0 as the phase at which the disc is eclipsed by the companion).

We therefore propose a warped, tilted and precessing disc as the origin for the variability of the X-ray modulation. Díaz Trigo et al. (2009) explained the appearance and disappearance of dips in XB 1254–690 as well as the changes in the optical emission by invoking a precessing warped disc, similar to the one in Her X-1 (Gerend & Boynton 1976). The existence of a warped disc in GX 13+1 together with a high inclination for the system would explain both the detection of a modulation in X-rays and the fact that the structure causing it is not phase-locked. Further, the warp would imply that the line of sight is slightly different at different phases, explaining the fact that we see different parts of the wind along the orbital period. The warp could have been caused by the disc wind, as in the case of Her X-1 (Schandl 1996) or simply by a critical illumination of the disc (Foulkes et al. 2010).

6. Conclusions

We find that:

- the disc wind in GX 13+1 originates at large radii, $\sim 10^{10}$ cm, and is consistent with being thermally driven, consistent with work by Ueda et al. (2004)
- the broad iron line can be explained by reprocessed emission in a hot atmosphere, and Compton scattering is the main source of its breadth
- contemporaneous changes of the broad iron line and the warm absorber point to an origin in the same disc wind. In particular, the broad iron line is too strong to be reproduced by reflection at the inner disc if we assume illumination from the boundary layer and reprocessing in a hot atmosphere, corona or wind illuminated by a harder, power-law-like, continuum is needed

- the presence of strong energy-dependent obscuration, found for first time in GX 13+1, and the absence of eclipses combined with the spectral type of the companion, indicate an inclination of 60–80°. The emission and absorption features expected in the disc wind scenario for such an inclination are consistent with the observed ones. This gives additional support to such scenario.

Acknowledgements. We thank an anonymous referee for useful comments. We thank Robin Corbet for providing us with the NIR light curves presented in Corbet et al. (2010). M. Díaz Trigo thanks Chris Done for useful discussions regarding optically thick winds and reflection models. Based on observations obtained with XMM-Newton, an ESA science mission with instruments and contributions directly funded by ESA member states and the USA (NASA). This research has made use of data obtained from the High Energy Astrophysics Science Archive Research Center (HEASARC), provided by NASA's Goddard Space Flight Center. We acknowledge support from the Faculty of the European Space Astronomy Centre (ESAC).

References

- Anders, E. & Grevesse, N. 1989, *Geochim. Cosmochim. Acta*, 53, 197
- Arnaud, K. A. 1996, in *ASP Conf. Ser. 101: Astronomical Data Analysis Software and Systems V*, 17
- Asai, K., Dotani, T., Nagase, F., & Mitsuda, K. 2000, *ApJS*, 131, 571
- Ballantyne, D. R. 2004, *MNRAS*, 351, 57
- Bandyopadhyay, R. M., Charles, P. A., Shahbaz, T., & Wagner, R. M. 2002, *ApJ*, 570, 793
- Bandyopadhyay, R. M., Shahbaz, T., Charles, P. A., & Naylor, T. 1999, *MNRAS*, 306, 417
- Begelman, M. C., McKee, C. F., & Shields, G. A. 1983, *ApJ*, 271, 70
- Boirin, L., Méndez, M. Díaz Trigo, M., Parmar, A. N., & Kaastra, J. 2005, *A&A*, 436, 195
- Boirin, L., Parmar, A. N., Barret, D., Paltani, S., & Grindlay, J. E. 2004, *A&A*, 418, 1061
- Cash, W. 1979, *ApJ*, 228, 939
- Corbet, R. H. D. 2003, *ApJ*, 595, 1086
- Corbet, R. H. D., Pearlman, A. B., Buxton, M., & Levine, A. M. 2010, *ApJ*, 719, 979
- Cottam, J., Kahn, S. M., Brinkman, A. C., den Herder, J. W., & Erd, C. 2001, *A&A*, 365, L277
- Den Herder, J. W., Brinkman, A. C., Kahn, S. M., et al. 2001, *A&A*, 365, L7
- Díaz Trigo, M., Parmar, A. N., Boirin, L., Méndez, M., & Kaastra, J. 2006, *A&A*, 445, 179
- Díaz Trigo, M., Parmar, A. N., Boirin, L., et al. 2009, *A&A*, 493, 145
- Done, C. & Díaz Trigo, M. 2010, *MNRAS*, 407, 2287
- Fabian, A. C. & Miniutti, G. 2005, *ArXiv Astrophysics e-prints*
- Fleischman, J. R. 1985, *A&A*, 153, 106
- Foulkes, S. B., Haswell, C. A., & Murray, J. R. 2010, *MNRAS*, 401, 1275
- Froning, C. S., Robinson, E. L., & Bitner, M. A. 2008, in *American Institute of Physics Conference Series*, Vol. 1010, *A Population Explosion: The Nature & Evolution of X-ray Binaries in Diverse Environments*, ed. R. M. Bandyopadhyay, S. Wachter, D. Gelino, & C. R. Gelino, 192–194
- García, J. & Kallman, T. R. 2010, *ApJ*, 718, 695
- García, J., Kallman, T. R., & Mushotzky, R. F. 2011, *ApJ*, 731, 131
- Gerend, D. & Boynton, P. E. 1976, *ApJ*, 209, 562
- Grindlay, J. E. & Seaquist, E. R. 1986, *ApJ*, 310, 172
- Hirano, T., Hayakawa, S., Nagase, F., & Masai, K. and Mitsuda, K. 1987, *PASJ*, 39, 619
- Homan, J., van der Klis, M., Wijnands, R., Vaughan, B., & Kuulkers, E. 1998, *ApJ*, 499, L41+
- Iaria, R., di Salvo, T., Lavagetto, G., D'Aí, A., & Robba, N. R. 2007, *A&A*, 464, 291
- Jansen, F., Lumb, D., Altieri, B., et al. 2001, *A&A*, 365, L1
- Juett, A. & Chakrabarty, D. 2006, *ApJ*, 646, 493
- Kaastra, J. S., Mewe, R., & Nieuwenhuijzen, H. 1996, in *UV and X-ray Spectroscopy of Astrophysical and Laboratory Plasmas*, ed. K. Yamashita & T. Watanabe, 411–414
- Kallman, T. & White, N. E. 1989, *ApJ*, 341, 955
- Kallman, T. R., Bautista, M. A., Goriely, S., et al. 2009, *ApJ*, 701, 865
- Laming, J. M. & Titarchuk, L. 2004, *ApJ*, 615, L121
- Laurent, P. & Titarchuk, L. 2007, *ApJ*, 656, 1056
- Lin, D., Remillard, R. A., & Homan, J. 2007, *ApJ*, 667, 1073
- Mason, K. O., Breeveld, A., Much, R., et al. 2001, *A&A*, 365, L36
- Matsuba, E., Dotani, T., Mitsuda, K., et al. 1995, *PASJ*, 47, 575
- Matt, G. 2006, *Astronomische Nachrichten*, 327, 949
- Miller, J. M., Maitra, D., Cackett, E. M., Bhattacharyya, S., & Strohmayer, T. E. 2011, *ApJ*, 731, L7
- Neilsen, J. & Lee, J. C. 2009, *Nature*, 458, 481
- Ng, C., Díaz Trigo, M., Cadolle Bel, M., & Migliari, S. 2010, *A&A*, 522, id.A96
- Paizis, A., Farinelli, R., Titarchuk, L., et al. 2006, *A&A*, 459, 187
- Parmar, A. N., Oosterbroek, T., Boirin, L., & Lumb, D. 2002, *A&A*, 386, 910
- Pozdnyakov, L. A., Sobol, I. M., & Sunyaev, R. A. 1979, *A&A*, 75, 214
- Proga, D. & Kallman, T. R. 2002, *ApJ*, 565, 455
- Reig, P., Papadakis, I., & Kylafis, N. D. 2003, *A&A*, 398, 1103
- Reynolds, C. S. & Nowak, M. A. 2003, *Physics Reports*, 377, 389
- Ross, R. R. & Fabian, A. C. 2005, *MNRAS*, 358, 211
- Schandl, S. 1996, *A&A*, 307, 95
- Schnerr, R. S., Reerink, T., van der Klis, M., et al. 2003, *A&A*, 406, 221
- Sidoli, L., Oosterbroek, T., Parmar, A. N., Lumb, D., & Erd, C. 2001, *A&A*, 379, 540

- Sidoli, L., Parmar, A. N., Oosterbroek, T., & Lumb, D. 2002, *A&A*, 385, 940
- Sim, S. A., Miller, L., Long, K. S., Turner, T. J., & Reeves, J. N. 2010a, *MNRAS*, 404, 1369
- Sim, S. A., Proga, D., Miller, L., Long, K. S., & Turner, T. J. 2010b, *MNRAS*, 408, 1396
- Stella, L., White, N. E., & Taylor, B. G. 1985, in *Proc. ESA Workshop: Recent Results on Cataclysmic Variables*, Vol. ESA SP-236, 125
- Stelzer, B., Wilms, J., Staubert, R., Gruber, D., & Rothschild, R. 1999, *A&A*, 342, 736
- Strüder, L., Briel, U., Dennerl, K., et al. 2001, *A&A*, 365, L18
- Sunyaev, R. A. & Titarchuk, L. G. 1980, *A&A*, 86, 121
- Tombesi, F., Cappi, M., Reeves, J. N., et al. 2011, *ApJ*, 742, 44
- Turner, M. J. L., Abbey, A., Arnaud, M., et al. 2001, *A&A*, 365, L27
- Ueda, Y., Asai, K., Yamaoka, K., Dotani, T., & Inoue, H. 2001, *ApJ*, 556, L87
- Ueda, Y., Murakami, H., Yamaoka, K., Dotani, T., & Ebisawa, K. 2004, *ApJ*, 609, 325
- Ueda, Y., Yamaoka, K., & Remillard, R. 2009, *ApJ*, 695, 888
- White, N. E. & Holt, S. S. 1982, *ApJ*, 257, 318
- White, N. E., Peacock, A., Hasinger, G., et al. 1986, *MNRAS*, 218, 129
- White, N. E. & Swank, J. H. 1982, *ApJ*, 253, L61
- Wilms, J., Allen, A., & McCray, R. 2000, *ApJ*, 542, 914
- Woods, D. T., Klein, R. I., Castor, J. I., McKee, C. F., & Bell, J. B. 1996, *ApJ*, 461, 767
- Xiang, J., Lee, J. C., Nowak, M. A., Wilms, J., & Schulz, N. S. 2009, *ApJ*, 701, 984